



WICHITA STATE
UNIVERSITY

UNIVERSITY LIBRARIES

Computational fluid dynamics study to develop pressure drop correlations for fluid flow through high porosity graphite foam as a function of microstructure parameters

Item Type	Thesis
Authors	Hegarty, Peter J.
Publisher	Wichita State University
Rights	Copyright 2016 by Peter J. Hegarty
Download date	2026-05-19 12:28:53
Link to Item	http://hdl.handle.net/10057/13506

COMPUTATIONAL FLUID DYNAMICS STUDY TO DEVELOP PRESSURE DROP
CORRELATIONS FOR FLUID FLOW THROUGH HIGH POROSITY GRAPHITE FOAM AS A
FUNCTION OF MICROSTRUCTURE PARAMETERS

A Thesis by

Peter J. Hegarty

Bachelor of Arts, Benedictine College, 2012

Bachelor of Science, University of North Dakota, 2012

Submitted to the Department of Mechanical Engineering
and the faculty of the Graduate School of
Wichita State University
in partial fulfillment of
the requirements for the degree of
Master of Science

December 2016

© Copyright 2016 by Peter J. Hegarty

All Rights Reserved

COMPUTATIONAL FLUID DYNAMICS STUDY TO DEVELOP PRESSURE DROP
CORRELATIONS FOR FLUID FLOW THROUGH HIGH POROSITY GRAPHITE FOAM AS A
FUNCTION OF MICROSTRUCTURE PARAMETERS

The following faculty members have examined the final copy of this thesis for form and content and recommend that it be accepted in partial fulfillment of the requirement for the degree of Master of Science, with a major in Mechanical Engineering.

Ikram Ahmed, Committee Chair

Tirivadi Ravigururajan, Committee Member

Klaus Hoffmann, Committee Member

DEDICATION

To my wife, Josie, whose
constant love and support
made this thesis possible

ACKNOWLEDGEMENTS

I would like to thank my committee members for their help and guidance. Also, thank you to all my professors throughout my academic career who have fostered my love of learning and discovery. Finally, thank you to my parents who gave me the greatest educational opportunities a person could hope for and allowed me to realize and achieve my academic goals.

ABSTRACT

In order to better understand the effect of microstructure parameters on forced convection pressure losses in graphite foam, correlations were developed for the permeability and form coefficient that appear in the porous media momentum equation. Computational fluid dynamics simulations were carried out for laminar, periodic air flow through an idealized pore geometry. Simulations were performed for foams with a wide range of pore diameter and inter-pore window diameter and porosity ranging from 0.75 to 0.85. The results of the simulations are validated using experimental results in literature within a certain range of values of the ratio of pore diameter to inter-pore window diameter. Expressions for the permeability and form coefficient as functions of pore diameter, inter-pore window diameter and porosity are developed using the results of the numerical simulations. To develop the permeability expression, an analogy was drawn to fully developed laminar flow through a pipe with an added term to account for the effect of porosity. To develop the form coefficient expression, it was assumed that the inertial effects on pressure drop are dominated by the ratio of the pore diameter to inter-pore window diameter. Terms to account for the effect of porosity were also added. The expressions are applicable within the ranges of Reynolds number, porosity, and pore diameter to inter-pore window diameter values that were validated. The proposed expressions are intended to be used in future studies related to the application of graphite foam in convective heat transfer applications.

TABLE OF CONTENTS

Chapter	Page
1 INTRODUCTION	1
1.1 Motivation	1
1.2 Objectives.....	2
2 LITERATURE REVIEW	4
2.1 Introduction to Graphite Foam.....	4
2.2 Experimental Studies of Flow through Graphite Foam	6
2.3 Numerical Studies of Flow through Graphite Foam	9
2.4 Advantages of Graphite Foam.....	12
2.5 Graphite Foam Microstructure	12
2.6 Porous Media Momentum Equation	15
2.6.1 Viscous Drag (Darcy) Term.....	17
2.6.2 Form Drag /Inertia/Forchheimer Term	19
2.6.3 Viscous Shear (Brinkman) Term	20
2.6.4 Advective (Convective) Inertial Term	21
2.6.5 General Porous Media Momentum Equation	22
2.6.6 Porous Media Reynolds Number	23
2.6.7 Porous Media Fluid Flow Regimes.....	25
3 GRAPHITE FOAM IDEAL GEOMETRY MODEL.....	27
3.1 Model Requirements	27
3.2 Evaluation of Previous Models	27
3.3 Proposal for New Model	31
4 NUMERICAL SIMULATIONS.....	39
4.1 Governing Equations.....	39
4.2 Discretization of the Continuity Equation.....	39
4.3 Discretization of the Momentum Equation	41
4.4 Gradient Evaluation.....	41
4.5 Pressure Interpolation Scheme and Pressure-Velocity Coupling.....	42
4.6 Solution Solver.....	42
4.7 Computational Domain and Boundary Conditions	43
4.8 Initial Conditions.....	46
4.9 Stability and Convergence	47
4.10 Grid Independence Study	47
4.11 Summary of Simulation Parameters.....	50
5 PREPARATION OF EXPERIMENTAL DATA	51

TABLE OF CONTENTS (continued)

Chapter	Page
6 RESULTS AND ANALYSIS.....	54
6.1 Model Validation.....	58
6.2 Pressure Drop Correlations	66
6.2.1 Permeability Model.....	67
6.2.2 Form Coefficient Model	72
6.2.3 Summary	76
7 CONCLUSION.....	78
8 FUTURE WORK.....	80
REFERENCES	82
APPENDICES	88
A. NUMERICAL RESULTS	89
B. COMPARISON OF NUMERICAL AND EXPERIMENTAL RESULTS	93

LIST OF TABLES

Table	Page
1. Foam microstructure parameters measured and reported in various studies involving experimental measurement of pressure drop in block graphite foam.	7
2. Porosity and surface area density expressions for various idealized geometry models to represent graphite foam microstructure from literature.	29
3. Percent difference between porosity and surface area density values predicted by Table 2 and the values predicted by 3D CAD model.	30
4. Comparison between porosity measured in Thompson experiment and porosity predicted by various ideal geometry models.	30
5. Porosity, surface area density and tortuosity expressions for the modified Druhma model used in the present study.	38
6. Grid Independence Study Results.....	48
7. Minimum number of cells required for each model to satisfy the mesh ratio requirement ($n=235$) from the grid independence study and the actual number of cells used in each model.	49
8. Summary of various parameters used for numerical simulations in Fluent.....	50
9. Experimental pressure drop data reported by Thompson [15] and transformed for use in validating numerical results.	53
10. Least-squares curve fit coefficient values with 95% confidence intervals resulting from fitting the experimental and numerical results to equation (4.3).	61
11. Ratio of pore diameter to window diameter of various models and its effect on the validity of the numerical simulations.	64
12. Permeability and form coefficient values with 95% confidence interval error values calculated from the least-squares regression analysis of the numerical results.	67
13. Results of multiple regression analysis using Microsoft Excel used to model the form coefficient as a function of porosity and pore diameter to window diameter ratio.	74
14. Summary of expressions for permeability and form coefficient of graphite foam as a function of foam geometry along with the limitations of these expressions.....	77
15. Pressure loss per unit length as a function of fluid velocity for the numerical results from the present study.	89

LIST OF FIGURES

Figure	Page
1. Comparison of (a) the traditional blowing technique for the production of carbon foams and (b) the process developed at Oak Ridge National Lab.	5
2. Scanning electron microscope image of mesophase pitch-derived graphite foam [1]	13
3. Various idealized geometry models used to represent graphite foam microstructure, (a) Yu’s cubic model, (b) Druhman’s BCC model, (c) Tee’s tetrakaidecahedron, (d) Sihn and Roy’s tetrahedron, and (e) Chai’s cubic model.	14
4. Cube diagonal cross section of (a) proposed modified Druhman model and (b) original Druhman model.....	33
5. Triangle used to calculate the maximum window diameter that is valid for modified Druhman model expressions.....	35
6. Average fluid particle path through idealized geometry model used in tortuosity calculation.	37
7. Control volume to illustrate discretization of scalar transport equations (f:cell face, c: cell center.....	40
8. Computational domain and boundary conditions	44
9. Grid independence study results using model 2A with 0.75 porosity	49
10. Experimental pressure drop in water column change per length as a function of Reynolds number reported by Thompson [15] used to validate numerical results of the present study.	51
11. Models with D_p/D_w values below 1.73 where the windows intersect each other, (a) 4B with $D_p/D_w=1.63$ and (b) 3C with $D_p/D_w=1.38$	55
12. Normalized pressure drop versus pore level Reynolds number from the numerical simulations. (a) Standard scale, (b) $\log_{10}(\text{Re}_h)$ scale to show Darcy flow region, standard scale for $0 < \text{Re}_h < 30$ to show transition from Darcy to inertial flow.....	57
13. Least-squares curve fit coefficient values with 95% confidence interval error bars resulting from fitting the experimental and numerical results to equation (4.3).	61
14. Numerical and experimental results for pressure gradient as a function of fluid velocity for sample 3B.....	63

LIST OF FIGURES (continued)

Figure	Page
15. Numerical and experimental results for pressure gradient as a function of fluid velocity for sample 4B.....	63
16. Numerical and experimental results for pressure gradient as a function of fluid velocity for sample 4A.	65
17. Plot of the permeability calculated using the numerical results as a function of the square of the hydraulic radius.....	68
18. Plot of the permeability calculated using the numerical results as a function of the square of the hydraulic radius divided by porosity raised to the power of 5.4.....	69
19. Residuals for the least-squares linear curve fit for the permeability model in equation (6.23).	70
20. Comparison of the dimensionless permeability of the proposed expression for graphite foam using an equivalent particle diameter with that of a packed bed of spherical particles.....	72
21. Plot of inertial coefficient from numerical results as a function of the ratio of pore to window diameter, Dp/Dw	73
22. Constant porosity curves for the proposed model as a function of pore to window diameter ratio overlaid with results from the numerical simulations.	75
23. Residual plots for each term in the multiple regression model for the form coefficient: (a) Dp/Dw , (b) ε , (c) $Dp/Dw * e$, and (d) $(Dp/Dw)^2$	75

LIST OF ABBREVIATIONS

CFD	Computational Fluid Dynamics
ORNL	Oak Ridge National Lab
RVC	Reticulated Vitreous Carbon
SEM	Scanning Electron Microscopy
TEM	Transmission Electron Microscopy

LIST OF SYMBOLS

A	Area (m ²)
a	Half the unit cube edge length in Druhma model (m)
\hat{b}	Least-squares linear curve fit coefficient
c_F	Form coefficient/ inertial coefficient / Forchheimer coefficient
d_p	Particle diameter (m)
d	Distance between sphere centers in Druhma model (m)
d_{mod}	Distance between sphere centers in modified Druhma model (m)
D_h	Hydraulic radius (m)
D_p	Pore Diameter (m)
D_w	Inter-pore window diameter (m)
D_{sq}	Inter-pore window diameter on square faces of tetrakaidecahedron unit cell
D_{hex}	Inter-pore window diameter on hexagonal faces of tetrakaidecahedron unit cell
e	Porous flow length in Darcy equation (m)
g	Acceleration due to gravity (m/s ²)
I	Identity vector
J	Mass flux (kg/m ² ·s)
K	Specific permeability (m ²)
K_D	Dimensionless permeability
k_H	Hydraulic conductivity in Darcy equation
k_k	Kozeny constant
L	Flow length (m)
N	Number of control volumes / cells

LIST OF SYMBOLS (continued)

n	Mesh ratio (N/D_h)
p	Pressure (Pa)
\mathbf{r}	Displacement vector
R^2	Linear regression correlation coefficient
s	Standard error
t	Time (s)
t_w	Wall thickness in modified Druhman model (m)
U	Macroscopic fluid velocity (m/s)
\mathbf{u}	Velocity vector
<u><i>Greek Letters</i></u>	
β	Surface area density (m^2/m^3)
ε	Porosity
Π_D	Dimensionless pressure gradient
ϕ	Scalar value
φ	Velocity potential
ρ	Density (kg/m^3)
σ	Pressure gradient of the linearly varying component in streamwise periodic flows
τ	Tortuosity
$\vec{\tau}$	Stress tensor
μ	Dynamic viscosity (Pa-s)
μ'	Effective dynamic viscosity (Pa-s)

LIST OF SYMBOLS (continued)

ν Kinematic viscosity, μ/ρ (m^2/s)

Mathematical Operators

∇ Gradient operator

∇^2 Laplace operator

CHAPTER 1

INTRODUCTION

1.1 Motivation

The power density required for cooling applications in various industries continues to rise due to advances in manufacturing and electronics and increased space constraints. This creates a need for thermal management devices that can provide improved heat transfer enhancement in a limited space. Compact heat exchangers are ideal for these applications since they have relatively high surface area-to-volume ratios and can transfer large amounts of heat in a small space.

The use of thermally conductive porous graphite foam to enhance heat transfer in compact heat exchangers has been the focus of several studies since the process used to make the graphite foam was developed in 1997. The material properties of graphite foam make it a very attractive alternative for heat transfer applications compared to more conventional porous media like sintered metals, packed beds, and metal foams. These properties include high thermal conductivity, large surface area-to-volume ratio, low density, low thermal expansion and resistance to corrosion. These properties make graphite foam ideal for heat transfer applications where size and weight limitations are critical, including electronic package cooling, and both terrestrial and space vehicle cooling and heating.

Some challenges that have prevented the widespread applications of graphite foam in heating and cooling applications is the high cost to produce the foam and the relatively large pressure drop associated with fluid flow through the foam. To address the large pressure drop, several studies have attempted to machine the foam into various shapes to reduce pressure drop while maintaining a high heat transfer rate. Relatively few studies have focused on reducing pressure losses by changing the microstructure of the foam. The few studies that have focused on

the effect of the microstructure on pressure drop have treated the graphite foam similar to other porous media, like metal foams and packed beds. Because the microstructure of graphite foam is different than any other previously studied porous media, all studies have been unable to provide a comprehensive evaluation of the effect of the microstructure on the pressure loss. A better understanding of the dependence of pressure losses on the microstructure parameters of graphite foam is required in order for graphite foam to be used in various applications.

1.2 Objectives

The goal of the present study is to develop correlations for pressure drop in graphite foam based on microstructure parameters, including the pore diameter, the inter-pore window diameter and the porosity. More specifically expressions will be developed for the permeability and form coefficient that appear in the momentum equation for porous media. These correlations will be derived from the results of computational fluid dynamics (CFD) simulations on foams of various pore diameter, inter-pore window diameter and porosity. The CFD simulations results will be validated using previous experimental data from literature.

The expressions for the pressure loss coefficients developed in the current study will allow for a more complete evaluation of graphite foam in various forced convection applications. Numerical simulations that model porous media in heat exchangers use a volume-average method that defines porous zones. The pressure loss coefficients that are the subject of this study are required inputs for these porous zones. The existence of expressions for these coefficients based on the foam microstructure will allow researchers to study the effect that the microstructure parameters have on the performance of heat exchangers. Further, specific combinations of pore diameter, window diameter and porosity can be tailored to specific applications. This comprehensive evaluation of the effect of microstructure parameters on heat exchanger

performance will allow for more widespread applications that can take advantage of the unique properties of graphite foam.

CHAPTER 2

LITERATURE REVIEW

2.1 Introduction to Graphite Foam

Graphite foam is a rigid porous material that is made up of a network of interconnected solid ligaments with spherical voids. It can have an open cell structure where the pores are connected, or a closed cell structure where pores are closed off from one another. Graphite foams are a specific type of carbon foams. The other types of carbon foams include reticulated vitreous (RVC) carbon foams and non-graphitic carbon foams. The different types of carbon foams are distinguished by the raw material or precursor used and the manufacturing process.

The first type of carbon foams produced were RVC foams in the 1960's. These foams were made by carbonizing thermosetting organic polymer foams through a simple heat treatment process [1]. In the early 1990's, researchers at Wright Patterson Air Force Base Materials Lab focused on producing a very structural and lightweight material with high specific strength that could replace expensive 3-D woven fiber preforms in polymer composites and honeycomb materials [1]. Their research led to the first mesophase-derived graphitic foams. The process used to create these foams involves a "blowing" technique applied to a melted pitch precursor. The foam is then oxidatively stabilized before carbonization and graphitization at elevated temperatures [2]. Researchers at West Virginia University sought to produce less expensive carbon foams by using inexpensive precursor materials such as coal, petroleum pitch, and coal tar pitch. Their process resulted in a carbon foams that were less expensive to produce but demonstrated excellent strength and thermal insulation properties [3].

A group at Oak Ridge National Lab (ORNL) developed a process in 1997 to make graphite foams that did not require the blowing or stabilization steps previously used. They instead used a

proprietary foaming technique. The differences between the process used at ORNL and the traditional “blowing” technique are shown in Figure 1. The removal of the blowing step saved time and the removal of the stabilization step improved the thermal conductivity of the final product [4]. This was the first process able to produce foams with bulk thermal conductivities exceeding 50 W/m·K [2]. The foam produced using this process has a graphitic structure and excellent bulk thermal conductivity (as high as 180 W/m·K) [5]. Graphite foam made using the three step process developed at ORNL is the topic of this paper.

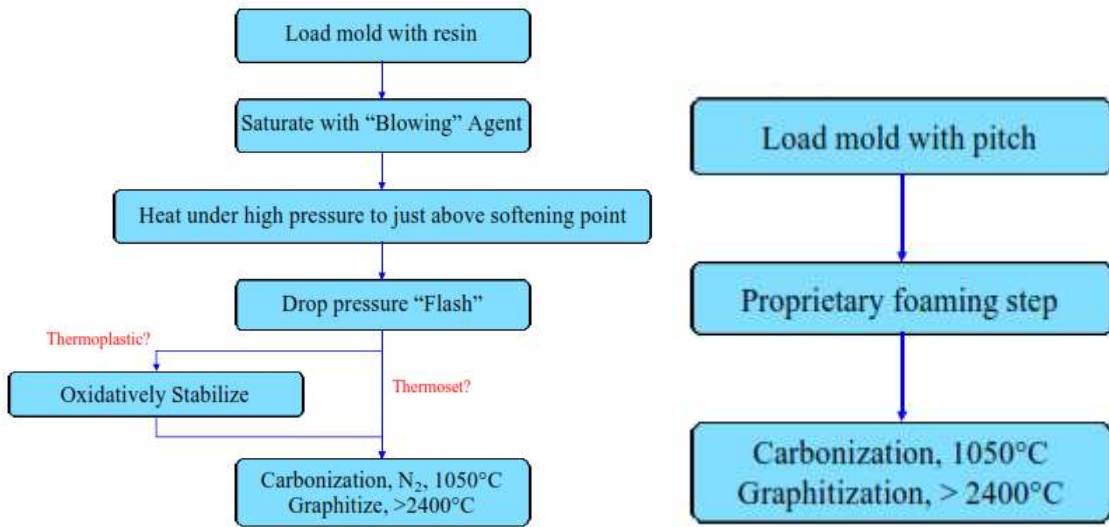


Figure 1. Comparison of (a) the traditional blowing technique for the production of carbon foams and (b) the process developed at Oak Ridge National Lab [2].

Klett et al. [1] provides a review of the process used to create graphite foam and the material properties that result. Examination of samples by optical image analysis, scanning electron microscopy (SEM), transmission electron microscopy, and X-ray diffraction revealed highly aligned graphitic structure in the foam, especially in the ligaments. A simple two parameter model was used to predict the thermal conductivity of the foam to within 5% of experimental measurements. The new model predicted the average thermal conductivity of the ligaments to be

greater than 1650 W/m·K at room temperature and 2300 W/m·K at liquid nitrogen temperatures. Bulk thermal conductivity as high as 180 W/m·K were measured in the vertical direction (during the foaming process) and 65 W/m·K in both in-plane directions (in horizontal plane). The higher conductivity in the vertical direction is attributed to the preferential orientation of graphite crystals in the vertical direction.

2.2 Experimental Studies of Flow through Graphite Foam

The use of graphite foam for heat transfer enhancement has been studied extensively. The majority of experiments have involved a fluid being forced through a certain foam geometry that is heated in some way on one side. A few studies attempted to setup a more complex system that more closely resemble a heat exchanger. The majority of experiments used air as the working fluid, and a few used water. Air is the preferred working fluid because graphite foam has low permeability and water requires a sealed channel to prevent leakage.

Several geometries of graphite foams have been tested for pressure drop and heat transfer properties. The simplest form, a rectangular block is able to transfer a large amount of heat from a given surface, but at the expense of high pressure losses. To address this issue several authors have tested a wide variety of geometries by machining the foam into a desired shape. These shapes include corrugated [2,6-9], finned [2,10], pin-finned [2], drilled holes [2,11], zig-zag [12], and baffled [12].

The most studied and most promising geometry that is not a block is the corrugated type. In this arrangement, channels with depth less than the thickness of the foam are cut with their length in the direction of flow, but not the full length of the sample. Compared to a block of foam, at certain flow rates the corrugated configuration has been shown to greatly reduce the pressure drop with a very small reduction in total heat transfer [7-8]. The corrugations significantly reduce

pressure loss by reducing the air penetration speed and shortening the distance the fluid must travel [7].

In any heat transfer device with graphite foam, whether it is a block or machined with channels or holes, there will always be fluid traveling through the interior pores of the foam. An accurate understanding of the behavior of a fluid in the foam microstructure is important for any configuration. Numerous authors [2,10,12-15] have measured heat transfer rate and pressure loss for flow through a block of foam. A list of these authors is in Table 1.

Table 1. Foam microstructure parameters measured and reported in various studies involving experimental measurement of pressure drop in block graphite foam.

Reference	Foam	Porosity		Pore Diameter		Window Diameter	
		Measured		Measured		Measured	
Thompson[15]	Multiple	Measured	0.75-0.85	Measured	350-1150	Measured	150-620
Leong[12]	Pocofoam	Measured	0.728	Measured	310	Not reported	--
Straatman[13]	Multiple	Measured	0.82-0.88	Measured	350-500	Not reported	--
Lin[6]	Pocofoam	Reported	0.75	Reported	350	Reported	110
Wu [14]	Pocofoam	Reported	0.70-0.80	Reported	350	Not reported	--
Gallego[2]	ORNL Foam	Not reported	--	Not reported	--	Not reported	--
Klett [10]	Pocofoam	Not reported	--	Not reported	--	Not reported	--

Lin et al. [6] conducted tests for heat transfer and pressure drop in a recuperative counter-flow heat exchanger with air flow through solid and corrugated Poco graphite foam blocks arranged in series. Heat exchanger effectiveness as high as 80% was achieved and the use of the corrugated block improved heat transfer and reduced pressure drop.

Thompson [15] measured heat transfer and pressure loss of air flow through a variety of graphite foam samples of varying pore diameters and inter-pore window diameters. The results showed a linear dependence of thermal performance (ratio of heat transfer to pressure drop) on the average inter-pore window diameter. Pressure drop was greatly reduced by increasing the pore and window diameter. The results were compared to aluminum finned heat exchangers and the specific heat transfer was an order of magnitude greater for the graphite foam, but the pressure drop was two orders of magnitude higher.

Gallego and Klett [2] tested foams of varying geometries (block, finned, pin-finned, blind holes) as a possible alternative heat sink material for electronics cooling with both air and water as the working fluid. The carbon foam heat sinks responded to transient loads significantly faster than traditional heat sinks and provided an effective heat sink material. In addition, modifying the geometry from block to corrugated and pin-finned greatly reduced the pressure drop while maintaining high heat transfer rates.

Leong [12] also measured pressure drop and heat transfer rates for airflow through a variety of graphite foam configurations, including block, zig-zag and baffled. A quadratic curve was fit to the pressure gradient curve for block foam to calculate the permeability and inertia/form coefficient for the graphite foam used. The block foam showed the best heat transfer performance, but the other configurations provided good heat transfer enhancement at a much lower pressure drop.

Wu et al. [14] showed that graphite foam is an advantageous solution for gas cooled condensers in cryogenic cooling applications compared to conventional heat sinks. The experiment used air with FC-87 refrigerant to simulate helium and gaseous/liquid hydrogen. The tests on both block and corrugated configurations showed that the carbon foam heat sinks can provide 18 times the heat transfer compared to conventional air channel heat sinks and moderate pressure drop at low speeds (~1 m/s).

Straatman et al. [13] measured the heat transfer rate and pressure drop for water flow through several samples of block graphite foam. The experimental data was used to calibrate a thermal non-equilibrium model to compare to aluminum foams. The graphite foam was able to transfer significantly more heat from a surface than the aluminum foams, but the aluminum foams were more permeable, resulting in lower pressure losses.

Klett [10] measured heat transfer and pressure drop of air flow through ORNL graphite foam with block and finned configurations. The results showed a tenfold increase in heat transfer compared to conventional radiators. He concluded that graphite foam would be an excellent choice in electronics and automotive cooling applications. Further, the use of graphite foam could significantly reduce heat exchanger size and could eliminate water as the cooling fluid and replace it with air in many applications.

2.3 Numerical Studies of Flow through Graphite Foam

There are two primary techniques available when performing numerical simulations of fluid flow through porous media: discrete modelling and the volume-averaged method. The first technique involves using a discretized model of the solid structure of the porous media and solving the Navier-Stokes equations in the fluid zones like any other standard CFD simulation. The volume-averaged method treats the porous media and fluid as a single continuum and uses local

volume-averaged forms of the governing equations. A more thorough description of these equations is provided in section 2.6. Both methods have advantages and disadvantages. The discrete modelling method is useful when the goal is to understand the effects of the local microstructure of the foam on the fluid flow. However, this method is limited to small-scale models of porous media and is not a realistic option for large-scale models like heat exchangers. The local volume-averaged method is the preferred method on large-scale models since the porous zone is modelled as a continuum. However, this method requires coefficients for pressure drop and heat transfer as inputs, which means the behavior of the fluid in the porous media must be understood beforehand. Both methods have been used to study fluid flow in graphite foam.

Leong [12] used experimental measurements of pressure drop to calibrate a numerical model that used the volume-averaged method with porous and open zones and the local thermal non-equilibrium method. The model was used to investigate various configurations of graphite foam, including zig-zag and baffled, and showed that these configurations achieve good heat transfer enhancement while reducing pressure drop.

Solmus [16] also used the volume-averaged method to investigate the heat transfer performance of block graphite foam at various flow rates and foam lengths. The results of the model agreed well with experimental data and showed that the graphite foam provided better heat transfer than the more conventional aluminum foam, but also resulted in higher pressure drop.

The method used to produce graphite foam often produces foam blocks with varying porosity in the vertical direction (during the foaming process). To address this, Betchen [17] used the volume-averaged method to study the influence of a linear porosity distribution on flow through graphite foam. The results showed that the effect of a porosity gradient on heat transfer was only significant at relatively high Reynolds numbers and that superior thermal performance

can be obtained by placing the more porous side of the foam block closest to the heat transfer surface.

Several authors have used a discretized model of graphite foam in numerical simulations. Karimian and Straatman [18] used the unit cube geometry model proposed by Yu [19] as the idealized internal structure of graphite foam and simulated periodic fluid flow with heat transfer in graphite foam for a range of porosities (75%-90%) and pore diameters (300-600 μm) to investigate the effect of the microscopic properties of the foam on pressure drop and heat transfer. The flow direction in the simulations was normal to the pore windows and the resulting flow field was similar to fully developed pipe flow at high flow rates, resulting in a pressure drop prediction that was significantly lower than experimental measurements. To address the low pressure drop, the same authors performed another study [20] where they investigated more generic multidirectional flow fields. The simulations produced better results, but the pressure drop was still lower than experimental measurements. Semi-heuristic models for pressure drop and heat transfer were presented based on the simulation results with additional factors that accounted for the differences with experimental results.

DeGroot [21] continued the work of Karimian and Straatman by performing direct numerical simulation using the same idealized geometry model proposed by Yu to obtain results for the relevant properties required to close the momentum and energy equations. The simulation results were used to compute the permeability and the non-Darcy drag term at various foam porosities and showed a non-linear relationship between the non-Darcy drag term and Reynolds number, which is in contradiction to the widely used Darcy-Forchheimer approach to modelling flow through graphite foam. The simulation results were not compared to experimental measurements.

2.4 Advantages of Graphite Foam

The advantages of graphite foam over conventional heat transfer surfaces is well documented. The foam's high thermal conductivity allows for quicker response times compared to conventional heat sinks [2]. In addition, graphite foams are superior to conventional surfaces like multi-louvered fins when there are space constraints and a high heat removal per unit volume is required [11]. Graphite foam heat sinks can be superior to conventional air heat sinks, especially at low flow rates [14].

The porous media that most closely resembles graphite foam is metallic foam. Graphite foam demonstrates several advantage over metallic foam. Not only is the bulk thermal conductivity of graphite foam greater than both aluminum and copper foams (180 W/m·K compared to 45 for copper [1]), but the density of the solid ligaments is lower. This results is a thermal conductivity-to-weight ratio (κ/ρ) greater than 200 W·m²/kg·K for graphite foams, compared to 45 W·m²/kg·K for copper foams [1]. Straatman [13] showed that graphite foam has higher heat transfer capability than aluminum foams at a given surface area. In addition, Garrity [11] showed that graphite foam is able to remove more heat per unit volume than both aluminum foams and multi-louvered fins.

2.5 Graphite Foam Microstructure

The manufacturing process used to create graphite foam creates a product with a complex microstructure. The resulting microstructure of a typical mesophase pitch-derived graphite foam is shown in Figure 2. The structure typically exhibits uniformly shaped pores with a fairly normal distribution. Inter-pore windows with diameters less than that of the pores are located where two pores intersect. The average pore size, orientation and distribution is primarily determined by the pitch viscosity and the foaming pressure [1]. The thickness of the solid ligaments is not uniform, but varies based on the arrangement of the pores. The graphitization step at temperature exceeding

2800°C results in highly aligned graphite crystals (see Figure 2) that give the foam its high thermal conductivity.

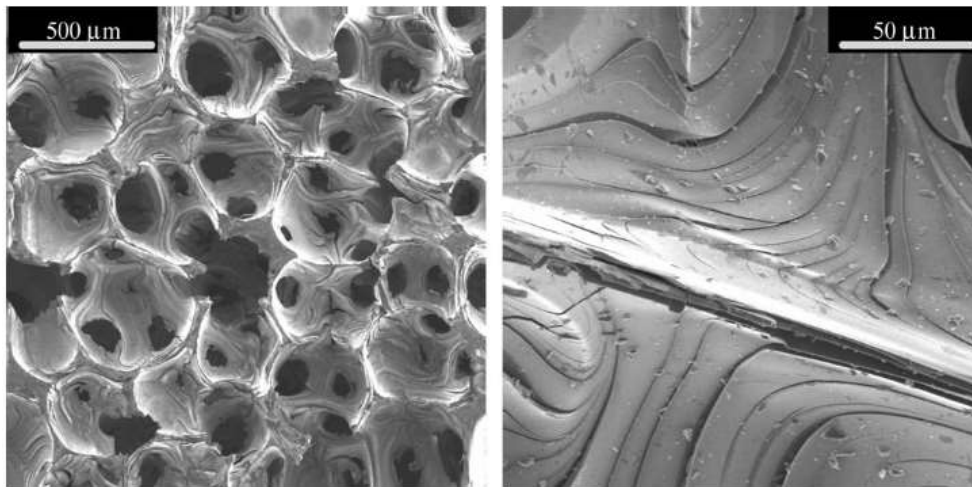


Figure 2. Scanning electron microscope image of mesophase pitch-derived graphite foam [1]

The complex microstructure of graphite foam makes studying the relationship between the microstructure properties and the thermal and hydraulic behavior of the foam very difficult. Several authors have attempted to represent graphite foam microstructure using idealized geometry models. All of the models offer a unique way to arrange the foam pores in space, which in turn affects how the inter-pore windows are arranged in space. The various models used for graphite foam are shown in Figure 3.

Yu et al.[19] represented the foam as a cube with a spherical void at the cube center and circular opening at each cube face. Druhna et al. [22-23] used a body centered cubic model that includes a cube with a single spherical pore at the center and eight additional pores of the same diameter centered at each corner of the cube. Tee et al. [24] modeled the foam using a tetrakaidecahedron unit cell. This shape consists of polyhedron with 14 faces, six that are square and eight that are hexagonal. The main pore is at the center with circular openings at each face.

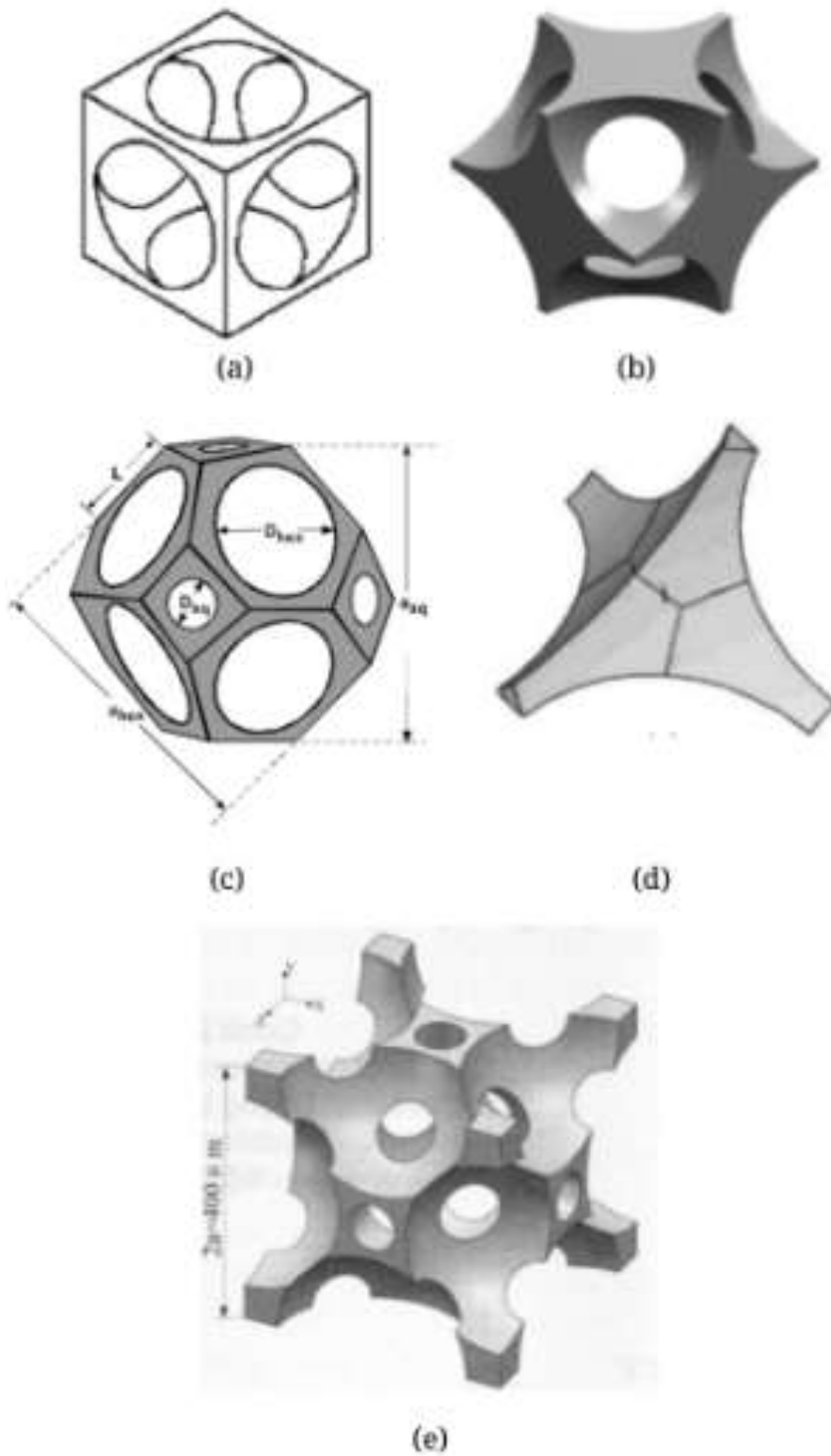


Figure 2. Various idealized geometry models used to represent graphite foam microstructure, (a) Yu's cubic model, (b) Druhman's BCC model, (c) Tee's tetrakaidecahedron, (d) Sihn and Roy's tetrahedron, and (e) Chai's cubic model.

Several authors, including Sihn and Roy[25], have used a simple tetrahedron model for graphite and metallic foams. This unit cell shape is formed by removing spherical pores from the 4 corners of a regular tetrahedron. Chai et al. [26] used a unit cube model with spherical pores centered at the cube center and at the midpoint of each cube edge. Chai's model also includes cylindrical holes in the center of each cube face.

The majority of the idealized geometry models have been used to develop correlations for the bulk thermal conductivity of graphite foam [19,23,24,26]. Only Tee [24] used an idealized geometry model to derive expressions for pressure drop and heat transfer as a function of microstructure. The model proposed by Yu [19] is the only model that has been used in numerical studies for pressure drop and heat transfer behavior. In addition to the thermal and pressure drop properties, several authors have used idealized geometry models to develop correlations for mechanical properties of graphite foam, including the modulus of elasticity, that are in good agreement with experimental measurements [25,27].

2.6 Porous Media Momentum Equation

In order to provide a review of pressure drop in porous media, a few concepts will be discussed. For a more comprehensive review of these concepts and others related to porous media see Kaviany [28] or Civan [29]. Some important terms related to pressure drop in porous media are porosity, tortuosity, local volume-averaging and non-Darcian effects.

The porosity of porous media is the volume fraction occupied by voids, or the total void volume divided by the total volume of the solid matrix [28]. The pores can be connected to multiple other pores (interconnected), connected to a single pore (dead end), or not connected to any other void (isolated). Fluid only flows through the interconnected pores. The effective porosity is the porosity of the interconnected pores. The porosity is equal to the effective porosity in non-

consolidated porous media like packed beds of particles. In some consolidated media, the two values can be different. The current study is concerned with the effective porosity of graphite foams, since this is property that affects fluid flow. Therefore, porosity and effective porosity will be used interchangeably for the remainder of the paper.

A fluid travelling through porous media does not travel in a straight path, but rather meanders around the solid matrix. The property that describes the extent of this meandering is the tortuosity. The tortuosity is traditionally defined as the length of the path a fluid particle will take between two points divided by the straight line distance between the points [28]. In reality, different fluid particles will have different path lengths through the matrix. The tortuosity describes the average flow length a particle will take.

Local volume-averaging is frequently used in investigations involving flow through porous media. The interaction between the fluid and the microstructure of porous media is complex and difficult to accurately predict. Because of this complexity at the microscopic scale, the transport processes of fluid flow through porous media are modelled in bulk at the macroscopic scale. The local volume-averaging process produces momentum and energy equations that treat the fluid and porous solid as a continuum.

Non-Darcian effects refer to a specific behavior of the pressure drop in porous media. These effects create a non-linear behavior of the pressure gradient with respect to fluid velocity. In Darcian flow, the relationship between fluid velocity and pressure gradient is linear, while non-Darcian effects create a non-linear (usually quadratic) relationship. The physical phenomena that cause this behavior will be discussed later.

The theory of fluid flow through porous media has a long and complex history. The evolution of the governing momentum equation, which is discussed extensively by Lage [30] is

evidence of this history. Nield [31] provides a review of modelling saturated porous media and discusses the individual terms of the modern porous media flow equations. The porous media momentum equation consist of the original viscous (Darcian) term, as well as several “non-Darcian” terms that have been added to account for effects that were previously neglected.

2.6.1 Viscous Drag (Darcy) Term

History

Henry Darcy pioneered the study of flow through porous media in 1856 during his research for the water supply system in Dijon, France [32]. Darcy performed experiments in which he measured the pressure drop of gravity induced water seepage through packed beds. The results showed that the pressure drop of the fluid flowing through the medium was linearly proportional to the macroscopic fluid velocity, which is the velocity the fluid would have, assuming the same mass flow rate, if the porous media were absent. The original Darcy equation has the form

$$k_H = U \frac{L}{\Delta p} \quad (2.1)$$

where k_H = Hydraulic conductivity
 U = Macroscopic fluid velocity
 L = Porous flow length
 p = Pressure

Additional contributions were made to form the modern version of the Darcy equation. First, the effect of temperature on the fluid properties was studied by Hazen in 1893 and Kruger added the dynamic viscosity to the equation in 1918 [33]. The modern form of the Darcy equation is

$$U = -\frac{K \Delta p}{\mu L} \quad (2.2)$$

where K is the specific permeability in square meters and μ is the dynamic viscosity. In the case of single phase flow, K is simply called the permeability. The permeability is a property of the geometry of the porous medium and is most-often independent of the fluid properties [32].

The Carman-Kozeny model is the most popular model used to define the permeability of porous media as a function of geometry. It was initially developed for creeping flow in packed beds of spherical particles, but several authors have proposed modifications and extensions of the basic expressions. One such extension, the Hagen-Poiseuille equation, uses the concept of hydraulic diameter to solve for the permeability in a packed bed [28]:

$$\frac{K}{d_p^2} = \frac{\varepsilon^3}{36k_K(1 - \varepsilon)^2} \quad (2.3)$$

where d_p is the mean or equivalent particle diameter and k_K is the Kozeny constant, which is a shape factor that represents the effect of the deviation of flow direction. The Kozeny constant is approximately 5 for packed beds, but is a strong function of porosity for other porous structures [28]. Several authors have extended the application of the Carman-Kozeny equation to porous media that does not resemble packed beds by using an equivalent diameter, D_e , which is the artificial spherical particle diameter required to preserve the surface area density of the pore structure. Using expressions for the area to volume ratio for packed beds, the equivalent particle diameter is

$$D_e = \frac{6(1 - \varepsilon)}{\beta} \quad (2.4)$$

where β is the surface area density, or surface area per unit volume.

Relevance to Present Study

The Darcy term in the porous media momentum equation accounts for the viscous shear stress the solid ligaments of the porous matrix impose on the fluid. This term is dominant in foams

with low permeability (on the order of 10^{-10} m^2) [34], but can become less dominant at lower permeability. Previous measurements of the permeability of graphite foam have been on the order of 10^{-10} m^2 [13]. The Darcy equation is limited to low Reynolds number flows (seepage flow) where inertial effects are negligible. The equation does not account for the no-slip condition imposed by a boundary of a porous media zone.

2.6.2 Form Drag /Inertia/Forchheimer Term

History

In 1863, Dupuit sought to explain the physics of Darcy’s law by using scientific principles [35]. He compared the flow through a permeable matrix with that of an open channel with a uniform velocity profile and proposed the following quadratic relationship:

$$-\frac{\Delta p}{\Delta x} = \alpha U + \gamma U^2 \quad (2.5)$$

where α and γ are determined experimentally and depend on both the porous geometry and fluid properties. In 1901, Forchheimer [36] performed experiments that confirmed the use of the quadratic equation over the previously accepted Darcy equation. Forchheimer is commonly credited with establishing the quadratic equation, and the quadratic form is often referred to as the “Darcy-Forchheimer” equation.

A more refined version of the quadratic equation known as the “Ergun Equation” was the result of an experimental study by Ergun [37] that focused on gas flow through crushed porous solids. It also revealed a second-order pressure drop relation that is commonly used to describe flow through packed beds. Ward [38] performed an extensive study on flow through porous media and proposed a relationship of the form

$$\left| \frac{\Delta p}{\Delta x} \right| = \frac{\mu U}{K} + \frac{c_F \rho U^2}{K^{1/2}} \quad (2.6)$$

where ρ is the fluid density and c_F is the form coefficient. Equation (2.6) is the most common form of the Darcy-Forchheimer equation. No physical reasoning was given for the placement of the $K^{1/2}$ in the quadratic term. However, since Ward's work, several studies have calculated K and c_F by curve fitting pressure drop versus velocity data and assuming the behavior in equation (2.6) to be true. A method for calculating the permeability and form coefficient is given by Beavers and Sparrow [39] and verified for fibrous media by Hunt and Tien [40], as well as others. Straatman [13] and Leong [12] used this method to calculate the permeability and form coefficient of graphite foam samples.

Relevance to Present Study

The form drag term was added to the Darcy term of the momentum equation. The effect of the form drag is noticed at relatively high Reynolds numbers. The most commonly proposed cause of this quadratic increase in pressure gradient is the form drag effects caused by the solid ligaments in the matrix. This effect is caused by the pressure drop across a blunt body in a fluid stream due to the wake that is formed on the downstream side of the body. The quadratic term becomes significant when the magnitude of the form drag is comparable to the viscous drag caused by the surface of the solid matrix. Various experimental studies show a nonlinear relationship between fluid velocity and pressure drop. These curves can be modelled with proper knowledge of the permeability, K , and the Forchheimer coefficient, c_F .

2.6.3 Viscous Shear (Brinkman) Term

History

In 1947, Brinkman [41] added a term to the Darcy equation to quantify the influence of the viscous shear stress that a solid surface of a high-permeability porous medium places on the fluid.

This is in addition to the effect of the viscous drag force that exists at the interface between the fluid and solid matrix as described by the Darcy term in the equation. With the inertial terms omitted, the equation takes the following form [28]:

$$\frac{\Delta p}{\Delta x} = -\frac{\mu}{K} \mathbf{u} + \mu' \nabla^2 \mathbf{u} \quad (2.7)$$

where μ' is the effective dynamic viscosity and \mathbf{u} is the velocity vector. The first term is the usual Darcy term and the second is analogous to the Laplacian term in the Navier-Stokes equation [32]. The inclusion of the Brinkman term is treated differently by various authors. Kaviany [28] provides a detailed review of the various ways to account for the Brinkman term as well as different expressions for the effective viscosity.

Relevance to Current Study

Nield [31] performed scale analysis that shows the relative magnitude of the Brinkman term compared to the Darcy term is on the order $O(K/L^2)$, where L is the characteristic length. The most common definition for the Darcy number is $Da=K/L^2$. The Brinkman term, therefore, becomes increasingly significant as the Darcy number approaches infinity and negligible as the Darcy number approaches zero. Since graphite foam is a relatively low-permeability porous media, the effect of the Brinkman term is negligible when modelling pressure drop for the current study.

2.6.4 Advective (Convective) Inertial Term

History

As explained by Nield [32], several authors have derived equations for porous media that are analogous to the Navier-Stokes equations and include an inertial term. One such form is shown in equation (2.8).

$$\rho \left[\frac{1}{\varepsilon} \frac{\partial \mathbf{u}}{\partial t} + \frac{1}{\varepsilon^2} (\mathbf{u} \cdot \nabla) \mathbf{u} \right] = -\nabla p - \frac{\mu}{K} \mathbf{u} \quad (2.8)$$

where ρ = Density of fluid
 ε = Porosity
 \mathbf{u} = Velocity vector
 t = Time

The $(\mathbf{u} \cdot \nabla) \mathbf{u}$ term is identical to the convective term in the Navier-Stokes equation. Several authors debate the significance of this term [31]. Joseph [42] argues that the advective term is negligible since the inertial effects are accounted for by the Forchheimer term. Some authors argue the term is necessary for prediction of the hydrodynamic boundary layer formation and entrance length, but Nield [32] discredits these notions by pointing out that the inclusion of this term is not a satisfactory way of expressing the nonlinear drag since $(\mathbf{u} \cdot \nabla) \mathbf{u}$ is zero for steady, incompressible, unidirectional flow.

Relevance to Current Study

The advective term, when compared to the Forchheimer drag term, scales on the order of $O(\sqrt{K}/c\varepsilon^2L)$. Since the permeability of graphite foam is relatively low, this term can be ignored [31].

2.6.5 General Porous Media Momentum Equation

Now that the history and relevance to the current study of the individual terms in the porous media momentum equation have been explained, a generally accepted equation that includes non-Darcian effects can be stated. Further, the form of the equation that applies to graphite foam in the current study can be stated.

Vafai and Tien [43] combined the work of Brinkman [41] and Muskat [44] and established local volume-averaged differential equations that include inertial effects and boundary effects in addition to the Darcy term in the momentum equation. Vafai and Kim [45] made refinements to

the equation in 1990. The resulting volume-averaged momentum equation for flow in porous media, known as the Brinkman-Forchheimer equation, is [28]

$$\rho \left[\frac{1}{\varepsilon} \frac{\partial \mathbf{u}}{\partial t} + \frac{1}{\varepsilon^2} (\mathbf{u} \cdot \nabla) \mathbf{u} \right] = -\nabla p + \mu' \nabla^2 \mathbf{u} - \frac{\mu}{K} \mathbf{u} - \frac{c_F \rho}{K^{1/2}} |\mathbf{u}| \mathbf{u} \quad (2.9)$$

where c_F is the Forchheimer (form) coefficient.

The appropriate equation for the present study, which involves steady, fully developed flow through low permeability porous media was derived by Joseph et al. [42] and restated by Nield and Bejan [32] as

$$-\nabla p = \frac{\mu}{K} \mathbf{u} + \frac{c_F \rho}{K^{1/2}} |\mathbf{u}| \mathbf{u} \quad (2.10)$$

2.6.6 Porous Media Reynolds Number

The definition of an appropriate Reynolds number for flow through porous media must be established so that the effect of this number on pressure drop can be understood. The general expression for Reynolds number is

$$\text{Re} = \frac{\rho L U}{\mu} \quad (2.11)$$

where L and U are some characteristic length and fluid velocity, respectively. The challenge in defining an appropriate Reynolds number is defining the length and velocity. Several authors, including Beavers and Sparrow [39], use the modified Reynolds number equation, which uses the square root of permeability as the length scale.

$$\text{Re}_K = \frac{\rho U K^{1/2}}{\mu} \quad (2.12)$$

The Reynolds number describes the ratio of inertial to viscous forces on the fluid. This is not necessarily appropriate to describe flow regimes in porous media. Because the pressure gradient in porous media is so much larger than in non-porous regions, the ratio of inertial to

viscous forces is no longer as important. Several authors, including Philipse [46] and Lage [47], argue that instead, the ratio of form drag to viscous drag imposed by the porous matrix on the fluid is more indicative of different flow regimes. Assuming quadratic pressure drop behavior in equation (2.10) the resulting Reynolds number is

$$Re'_K = \frac{\text{form drag}}{\text{viscous drag}} = \frac{c_F \rho U^2 / K^{1/2}}{\mu U / K} = \frac{c_F \rho U K^{1/2}}{\mu} \quad (2.13)$$

Another approach to define Reynolds number is the use of the hydraulic radius model proposed by Carman [48]. This model uses hydraulic radius, D_h as the length scale.

$$D_h = \frac{4 * \text{void volume}}{\text{wetted surface area}} \quad (2.14)$$

For foams with porosity ε and surface area density β this results in

$$D_h = \frac{4\varepsilon}{\beta} \quad (2.15)$$

Along with the hydraulic diameter as the length scale, the average pore-level velocity, U_p can be used:

$$U_p = \frac{U\tau}{\varepsilon} \quad (2.16)$$

where τ is the tortuosity of the porous media. Using D_h and U_p for L and U in equation (2.11) results in the following expression for Reynolds number.

$$Re_H = \frac{4\rho U\tau}{\beta\mu} \quad (2.17)$$

Application to Current Study

Calculating the Reynolds number using equation (2.13) requires knowledge of the permeability and form coefficient for the porous media in question. The advantage of the Reynolds number expressed in equation (2.17) is that the only necessary foam properties required as inputs

are the surface area density and tortuosity, which can be easily estimated if the pore diameter, window diameter, and porosity are known. Using equation (2.13) requires knowledge of the permeability and form coefficient which must be calculated experimentally. The expression in equation (2.17) will be used for the Reynolds number in the present study.

2.6.7 Porous Media Fluid Flow Regimes

Dybbs and Edwards [49] performed studies on packed beds of spheres as well as complex arrangements of cylinders and observed the three dimensional velocity distribution using dye streak lines. They define a Reynolds number based on average pore-level velocity and an average length scale of the pores. Four distinct flow regimes were defined based on their observations [28].

- $Re < 1$, Darcy or creeping flow regime: The viscous forces dominate over the inertial forces and only the local pore level geometry influences the flow.
- $1-10 < Re < 150$, Inertial flow regime: Steady nonlinear, or inertial, laminar flow begins between a Reynold number of 1 and 10. Boundary layers become more pronounced and uniform velocity regions are present. These regions become larger as Re is increased and the boundary layer decreases, indicating the dominance of inertial force over the viscous force.
- $150 < Re < 300$, Unsteady laminar flow regime: Oscillations on the order of 1 Hz and with amplitudes on the order of one-tenth the pore diameter are observed. No local dispersion of the dye is observed, indicating the flow is still laminar.
- $Re > 300$, Unsteady and chaotic flow regime: The flow is no longer laminar and turbulent mixing appears. At high Re numbers, the normalized pressure drop does not change with Reynolds number. This asymptotic behavior is reached for Re between 10^3 and 10^4 .

Application to Current Study

In turbulent flow through porous media, the pressure gradient diverts from the quadratic behavior in equation (2.10). In addition, at very low Reynolds numbers, the inertial effects on pressure drop are negligible. The present study is only concerned with the Reynolds number range where the pressure gradient is quadratic and can be described by equation (2.10). Therefore, the current study will focus on flow with Reynolds numbers (as defined by equation (2.17)) between 10 and 300.

CHAPTER 3

GRAPHITE FOAM IDEAL GEOMETRY MODEL

This chapter explains the development of the idealized geometry model used to model graphite foam for the numerical simulations. The requirements for the model are explained, then various models from literature are reviewed as possible options for the model. Finally, a modified version of a model from literature that satisfies the requirements is proposed as the model to use for the simulations.

3.1 Model Requirements

The goal of the present study is to develop pressure drop correlations for flow through graphite foam based on pore diameter, inter-pore window diameter, and porosity using computational fluid dynamics (CFD) simulation results. The first step in this solution is choosing an idealized geometry model to use in the numerical simulations. The model must satisfy the following criteria:

1. The geometry model must reflect the general microstructure of graphite foam, especially parameters that affect fluid flow such as porosity, tortuosity, pore diameter and window diameter.
2. The CFD model will be validated using the experimental results from Thompson [15]. Therefore, the geometry model must be validated by the microstructure parameters measured in the experiment, which include pore diameter, inter-pore window diameter, and porosity.

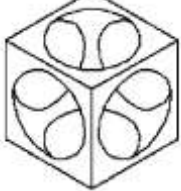


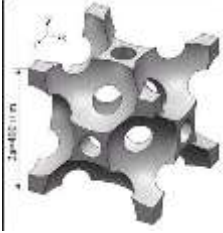
3.2 Evaluation of Previous Models

The geometry models described in section 2.5 are considered as possible options to use in the simulations. Applying the second criteria, the tetrakaidecahedron proposed by Tee is

eliminated since it requires two unique window diameters for the square and hexagonal faces. Applying the same criteria, the model proposed by Chai is only an option if the hole in the center of each face is removed. The remaining models to be considered as options for the CFD model include those of Yu, Druhman and Chai, and the tetrahedron. The three parameters these models share is porosity, pore diameter, and inter-pore window diameter. For each model, any two of these are independent variables, and the remaining parameter is the dependent variable. All three variables were measured in the Thompson experiment. Applying the first criteria, each model will be evaluated by how accurately it predicts the porosity of each sample in the Thompson experiment given the pore diameter and inter-pore window diameter as inputs. To do this, expressions for each model must be presented.

Yu et al.[19] provide expressions for their model relating the porosity and surface area density to the pore diameter and window diameter based on the unit cube length, H . These expressions are only valid when the structure is continuous and when the pores are interconnected. Druhman et al. [22] also present expressions for porosity and surface area density based on the pore and window diameters and the distance between the center and corner pored, d . The model is limited to cases where the pores are interconnected and the corner spheres are connected with the center sphere only and not with each other. Sihn and Roy [25] did not report expression for porosity and surface area density, so these expressions were derived. The expressions are valid when the pore diameter is small enough so that the pores do not meet in the center of a face. Chai et al. [26] did not report expressions for porosity and surface area density so they were also derived. The distance, a , is half the edge length of the unit cube. The expressions are valid when the spheres are large enough to be interconnected but not large enough so that the structure becomes disconnected. The expressions and limitations for these models are summarized in Table 2.

Table 2. Porosity and surface area density expressions for various idealized geometry models to represent graphite foam microstructure from literature.

Model	Condition(s)	Expressions	Equation
Yu 	$1011 < D_w < H$ $0.52 < \varepsilon < 0.96$	$H^3 - \frac{3\pi D_p^2}{4\varepsilon + \pi} H + \frac{4\pi D_p^3}{3(4\varepsilon + \pi)} = 0$	(3.1)
		$\beta = \frac{\pi D_p}{H^3} (3H - 2D_p)$	(3.2)
		$H = \sqrt{D_p^2 - D_w^2}$	(3.3)
Druhna 	$d < D_p \leq \frac{2d}{\sqrt{3}}$ $0.68 < \varepsilon < 0.94$	$\varepsilon = \frac{\sqrt{3}\pi}{8d^3} (6D_p^2 d - 3D_p^3 - 2d^3)$	(3.4)
		$\beta = \frac{3\sqrt{3}\pi D_p (4d - 3D_p)}{4d^3}$	(3.5)
		$d = \sqrt{D_p^2 - D_w^2}$	(3.6)
Tetrahedron 	$D_p > 2D_w$ $D_w > 0$ $0.78 < \varepsilon < 0.99$	$\varepsilon = \frac{\pi D_p^3 / 4.030 - 3.250\pi h \left(\frac{3}{4} D_w^2 + h^2 \right)}{(D_p^2 - D_w^2)^{3/2}}$	(3.7)
		$\beta = \frac{1.489\pi D_p (D_p - 13.397h)}{(D_p^2 - D_w^2)^{3/2}}$	(3.8)
		$h = \frac{1}{2} \left(D_p - \sqrt{D_p^2 - D_w^2} \right)$	(3.9)
Chai 	$D_p > \sqrt{2}a$ $\sqrt{\frac{2}{3}}a > D_w > 0$	$\varepsilon = \frac{3\pi D_p}{8a^2} \left(\frac{2\sqrt{2}a^2}{3D_p} + \frac{\sqrt{2}D_w^2}{D_p} + \sqrt{2}D_p - \frac{D_w^2}{a} - 2a - \frac{D_p^2}{9a} \right) + \frac{3\pi D_f^2}{16a^3} \left(a - \frac{D_p}{2} \right)$	(3.10)
		$\beta = \frac{\pi D_p}{2a^3} (6\sqrt{2}a - 5D_p) + \frac{\pi D_f}{16a^3} (4a - 2D_p - D_f)$	(3.11)
		$a = \sqrt{\frac{1}{2} (D_p^2 - D_w^2)}$	(3.12)

The expressions in Table 2 were validated by comparing their predicted values for porosity and surface area density with values predicted from a 3D CAD model. CAD models in CATIA were created for three of the samples mentioned in Thompson’s paper [15] and measurements were made using CATIA. The results of this validation study are in Table 3.

Table 3. Percent difference between porosity and surface area density values predicted by Table 2 and the values predicted by 3D CAD model.

Experiment			Yu		Druhman		Tetrahedron		Chai	
Sample	D _p (μm)	D _w (μm)	ϵ	β	ϵ	β	ϵ	β	ϵ	β
2A	342	157	0.009	0.001	0.000	0.002	0.304	0.021	-0.003	0.014
3A	491	222	0.006	0.000	0.001	-0.001	0.23	0.001	0.000	-0.026
4A	1004	360	-0.004	-0.012	0.001	-0.006	0.089	0.002	0.003	-0.001

Table 1. Comparison between porosity measured in Thompson experiment and porosity predicted by various ideal geometry models.

Experiment				Predicted Porosity			
Sample	D _p (μm)	D _w (μm)	Reported Porosity	Yu	Druhman	Chai	Tetrahedron
2A	342	157	0.75-0.85	0.71	0.90	0.94	0.98
3A	491	222		0.70	0.89	0.94	0.98
3B	633	372		0.84	n/a	n/a	n/a
3C	405	293		n/a	n/a	n/a	n/a
4A	1004	360		0.63	0.81	0.87	0.92
4B	849	522		0.87	n/a	n/a	n/a
4C	1159	612		0.77	0.96	n/a	n/a

*Values with n/a result in disconnected structure and are not considered valid.

The results in Table 3 prove that the expressions in Table 2 are valid. Therefore, these expressions can be used to predict the porosity of all the samples used in Thompson's paper [15] using the measured pore diameter and window diameter as inputs. Table 4 shows a comparison between the porosity reported (and measured) in the Thompson experiment and the porosity predicted by each ideal geometry model being considered. The model that predicts porosities closest to the experimentally measured porosity is Yu's cubic model. However, even though Yu's model is the best at predicting the porosity, it does not accurately reflect the tortuous path a fluid must take through foam. If repeating blocks of Yu's model are placed one after another, the fluid will simply pass through each window in a straight path with little resistance. This problem has been documented by previous numerical studies, where the use of Yu's model resulted in pressure losses far below experimental values [20-18]. The second best model at predicting the correct porosity is Druhman's model. This model more accurately reflects the tortuosity of graphite foam compared to Yu's model. Druhman's model, however, is less than ideal since it predicts porosities that are above the measured range for all but one sample and the structure becomes disconnected for other samples.

3.3 Proposal for New Model

To address the shortcomings of Druhman's model, a modified version is proposed. The original model has sharp corners at the inter-pore windows where the pore spheres intersect. The modified model is the same as the original except there is now a thickness at the windows instead of a sharp edge. In the original model, with a given pore diameter and window diameter, the window diameter will decrease if the pores are moved further apart. However, if a cylindrical hole with diameter equal to the window diameter is drilled between spheres, the spheres are able to move further apart without changing the window diameter. Instead, what changes is the thickness

of the windows and the porosity. This modified model has three independent variables and a fourth dependent variable (the added variable is the window thickness). With the addition of the thickness as a parameter, at a given pore and window diameter, the thickness can be adjusted until the desired porosity is reached. For the samples in the Thompson experiment, the thickness in the modified model can be adjusted until the porosity matches the measured value. This modified version of Druhman's model satisfies both criteria required for the CFD model and will be used for the CFD simulations.

Expressions similar to those in Table 2 must be derived for the modified version of Druhman's model. Like the original model, the case is considered when the corner spheres are connected with the center sphere only and not with each other. First, equation (3.4) is modified by separating the void volume and total volume. If the length of the unit cube edge of the original model is $2a$ and the distance between the corner and center of the cube is d , then $a = d/\sqrt{3}$. The total volume of the unit cube for the original model is

$$V_{total} = 8a^3 = \frac{8d^3}{3\sqrt{3}} \quad (3.13)$$

Now, equation (3.4) can be written in terms of the void volume over the total volume.

$$\varepsilon = \frac{V_{void}}{V_{total}} = \frac{\pi \left(2D_p^2 d - D_p^3 - \frac{2}{3} d^3 \right)}{\frac{8d^3}{3\sqrt{3}}} \quad (3.14)$$

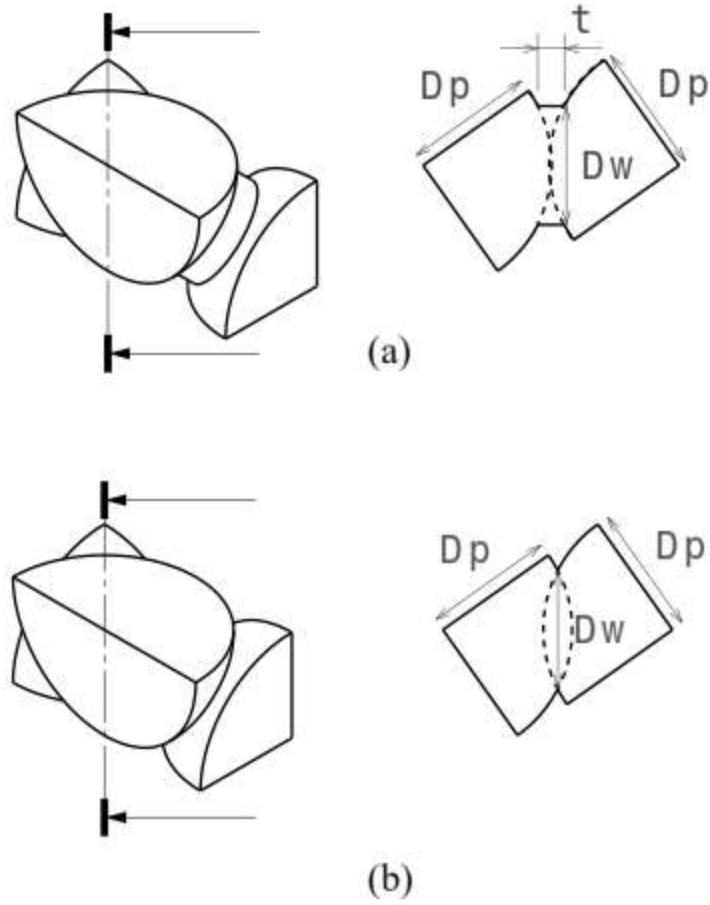


Figure 4. Cube diagonal cross section of (a) proposed modified Druhma model and (b) original Druhma model

In the modified model a new parameter, t_w , is introduced as the thickness of the inter-pore windows at the cube diagonals as seen in Figure 4. The distance between spheres must be modified to account for this thickness.

$$d_{mod} = d + t_w \quad (3.15)$$

The new total volume of the unit cube is

$$V_{total,mod} = \frac{8d_{mod}^3}{3\sqrt{3}} = \frac{8(d + t_w)^3}{3\sqrt{3}} \quad (3.16)$$

The additional void space that exists in the modified model is the volume of the inter-pore window cylinders. To simplify the expressions, the top and bottom of these cylinders are assumed to be planar. In reality, the cylinders intersect the sphere surface and are not planar at each end. The validity of this assumption will be checked later. Since there are 8 inter-pore windows in each unit cube, the added volume from these cylinders and total void volume are:

$$V_{added} = 8V_{cylinder} = 8 \left(\frac{\pi D_w^2}{4} t_w \right) = 2\pi D_w^2 t_w \quad (3.17)$$

$$V_{void,mod} = \pi \left(2D_p^2 d - D_p^3 - \frac{2}{3} d^3 + 2D_w^2 t_w \right) \quad (3.18)$$

Using equation (3.6), $V_{void,mod}$ can be written in terms of D_p and d only. The final expression for porosity in equation (3.28) is found by dividing equation (3.18) by equation (3.16).

An expression for the surface area density of the modified model can be found using a similar approach as with the porosity expression. Equation (3.5) is manipulated so separate the total volume and the surface area of the original model.

$$\beta = \frac{A_s}{V_{total}} = \frac{2\pi D_p (4d - 3D_p)}{\frac{8d^3}{3\sqrt{3}}} \quad (3.19)$$

Once again, the assumption of planar cylindrical faces for the inter-pore window cylinders is used.

The added surface area that these cylinders provide is:

$$A_{s,added} = 8(\pi D_w t_w) \quad (3.20)$$

The final expression for surface area density of the modified model in equation (3.29) is found by adding equation (3.20) to the numerator in equation (3.19) and dividing by equation (3.16).

These expressions for porosity and surface area density have several limitations. First, they are limited to cases where the window diameters are small enough that they do not intersect one

another. The diameters start to intersect when the window cylinder no longer fits inside the sphere quadrant of diameter D_p . A cylinder with the maximum diameter that fits inside a spherical quadrant will touch the midpoints of the three arcs in the quadrant. When this condition is met the triangle in Figure 5 can be used to calculate the cylinder diameter (which is the window diameter) in terms of the pore diameter. In Figure 5, the bottom corners of the triangle are points where the window cylinder touches the spherical quadrant arc midpoints and the top corner is the center of the window.

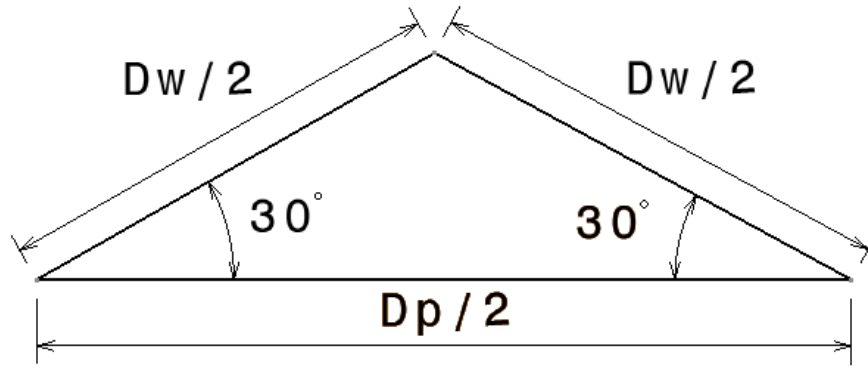


Figure 5. Triangle used to calculate the maximum window diameter that is valid for modified Druhna model expressions.

Using Figure 5 and the law a sines, the following limitation is places on the modified Druhna model:

$$D_w \leq \frac{D_p}{\sqrt{3}} \quad (3.21)$$

Another way of stating this is that the ratio D_p/D_w must be greater than $\sqrt{3}$, or 1.73. The other limitation on the expressions for the modified model is that the pores must be interconnected, or

$$D_w > 0 \quad (3.22)$$

The expressions are also only valid for the case where the corner pores do not intersect one another at the cube faces, or

$$D_p \leq \frac{2(d + t_w)}{\sqrt{3}} \quad (3.23)$$

The expressions for porosity and surface area density of the proposed modified Druhna model as well as the limitations for these expressions are summarized in Table 5.

Like the expressions in Table 2, the expressions for porosity and surface area density were validated by comparing the predicted values for porosity and surface area density for each model to the values measured from a 3D CAD model in CATIA. The difference between the 3D CAD measurements and the expressions was less than one percent for all models. The small difference is likely caused by the assumption that the tops and bottoms of these cylinders are planar, as mentioned earlier. The small difference shows that this assumption is valid for the models used.

In order to calculate the Reynold's number using equation (2.17), the tortuosity of the foam must be known. In order to develop a correlation for the tortuosity of the proposed model, a simplified path through the unit cell will be used to represent the average fluid particle path. This path, shown in Figure 6, goes from the centroid of the circle quadrant (point 1) to the center of the cylindrical face representing the window (point 2), through the center of the cylinder to point 3, then to the centroid of the circle quadrant at the midpoint of the unit cell (point 4). The reverse of this path is repeated to reach the end of the unit cell. The actual fluid path through the unit cell will be more complex with various curvatures, but this simplified path allows for expressions to be developed and captures the effect of the microstructure on the tortuosity.

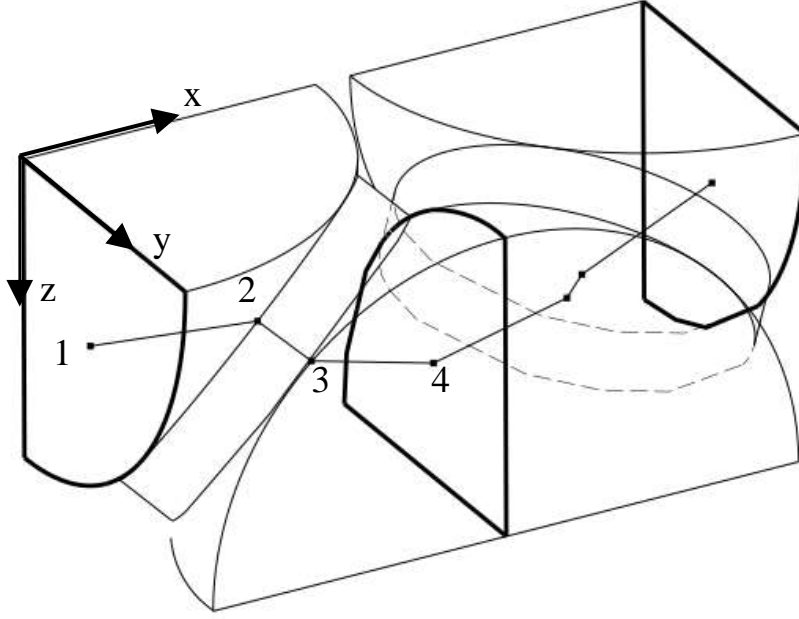


Figure 6. Average fluid particle path through idealized geometry model used in tortuosity calculation.

Using the symmetries in the model it can be seen that the length L_{1-2} is equal to L_{3-4} . Also the length L_{2-3} is simply the window thickness, t_w . The length L_{1-2} must be known to calculate the tortuosity. The position vector components of the quadrant centroid at point 1 in the coordinate system shown in Figure 6 are $r_{1z} = r_{1y} = 2D_p/3\pi$ [50] and $r_{1x} = 0$. The components of point 2 at the center of the cylinder face are $r_{2x} = r_{2y} = r_{2z} = \frac{a}{2} = \frac{d}{2\sqrt{3}}$. The magnitude of the vector between these points is

$$L_{1-2} = \sqrt{(r_{2x} - r_{1x})^2 + (r_{2y} - r_{1y})^2 + (r_{2z} - r_{1z})^2} \quad (3.24)$$

or

$$L_{1-2} = \sqrt{2\left(\frac{d}{2\sqrt{3}} - \frac{2D_p}{3\pi}\right)^2 + \frac{d^2}{12}} \quad (3.25)$$

If the length of the half unit cell is $(d + t)/\sqrt{3}$ the tortuosity is


$$\tau = \frac{\sqrt{3}(2L_{1-2} + t_w)}{(d + t_w)} \quad (3.26)$$

or

$$\tau = \frac{\left[24\left(\frac{d}{2\sqrt{3}} - \frac{2D_p}{3\pi}\right)^2 + d^2\right]^{1/2} + t_w}{(d + t_w)} \quad (3.27)$$

The expression for tortuosity along with the other expressions for the proposed model are summarized in Table 5.

Table 5. Porosity, surface area density and tortuosity expressions for the modified Druhma model used in the present study.

<p>Modified Druhma</p> 	$0 < D_w \leq \frac{D_p}{\sqrt{3}}$ $D_p \leq \frac{2(d + t_w)}{\sqrt{3}}$	$\varepsilon = \frac{3\sqrt{3}\pi}{8(d + t_w)^3} \left(2D_p^2d - D_p^3 - \frac{2}{3}d^3 + t_w(2D_p^2 - 2d^2) \right) \quad (3.28)$
		$\beta = \frac{3\sqrt{3}\pi \left(4D_p d - 3D_p^2 + 4t_w \sqrt{D_p^2 - d^2} \right)}{4(d + t_w)^3} \quad (3.29)$
		$d = \sqrt{D_p^2 - D_w^2} \quad (3.30)$
		$\tau = \frac{\left[24 \left(\frac{d}{2\sqrt{3}} - \frac{2D_p}{3\pi} \right)^2 + d^2 \right]^{1/2} + t_w}{(d + t_w)} \quad (3.31)$

CHAPTER 4

NUMERICAL SIMULATIONS

All simulations were done assuming steady, incompressible and three-dimensional flow using Ansys Fluent. The governing equations defining the physics of the flow are briefly described in the following sections. Next, an overview of the methods used to discretize and solve the governing equations is presented.

4.1 Governing Equations

The incompressible, steady-state, constant viscosity, non-conservative form of the Navier-Stokes continuity and momentum equations are invoked by Fluent and are shown in equation (4.1) and equation (4.2) [51].

$$\text{Continuity:} \quad \nabla \cdot \mathbf{u} = 0 \quad (4.1)$$

$$\text{Momentum:} \quad (\mathbf{u} \cdot \nabla)\mathbf{u} + \frac{\nabla p}{\rho} = \nu \nabla^2 \cdot \mathbf{u} \quad (4.2)$$

where \mathbf{u} = Velocity vector

ν = Kinematic viscosity = μ/ρ

p = Pressure

The equations above assume no body forces on the fluid.

4.2 Discretization of the Continuity Equation

The continuity equation can be written in integral form as:

$$\oint \rho \mathbf{u} \cdot d\mathbf{A} = 0 \quad (4.3)$$

where \mathbf{A} is the surface area vector. Integrating over the control volume for all faces in Figure 7 results in the following discrete form of the equation:

$$\sum_f^{N_{faces}} J_f A_f = 0 \quad (4.4)$$

where f is the face number, J the mass flux and A the face area. This equation is used to correct the values of pressure, velocity and face mass flux.

Fluent uses a momentum-weighted averaging technique to evaluate the velocity at cell faces in reference to the values at cell centers. Using this method, the mass flux through each face is expressed as

$$J_f = \hat{J}_f + d_f(p_{c0} - p_{c1}) \quad (4.5)$$

where p_{c0} and p_{c1} are the pressures in the two cells on either side of the face, \hat{J}_f contains the influence of velocities in these cells, and d_f is a function of the average momentum equation coefficients for the cells on either side of the face.

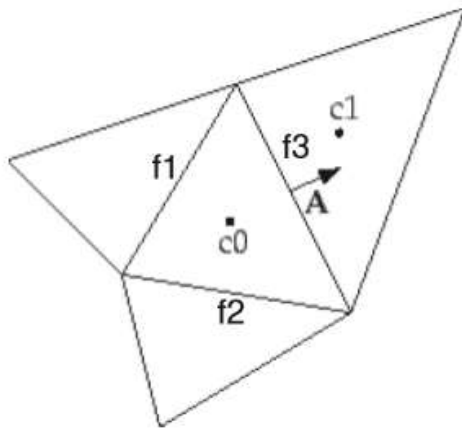


Figure 7. Control volume to illustrate discretization of scalar transport equations (f:cell face, c: cell center)

4.3 Discretization of the Momentum Equation

The x-momentum equation can be written in integral form as:

$$\oint \mathbf{J}\mathbf{u} \cdot d\mathbf{A} = - \oint p\mathbf{l} \cdot d\mathbf{A} + \oint \vec{\tau} \cdot d\mathbf{A} \quad (4.6)$$

where $\vec{\tau}$ is the stress tensor. Just like the continuity equation, integrating over the control volume for all faces in Figure 7 results in the following discrete form of the equation:

$$\sum_f^{N_{faces}} \mathbf{J}_f \mathbf{u}_f \cdot \mathbf{A}_f = - \sum_f^{N_{faces}} p_f \mathbf{l} \cdot \mathbf{A}_f + \sum_f^{N_{faces}} \vec{\tau}_f \cdot \mathbf{A}_f \quad (4.7)$$

This form of the discretized momentum equation applies to multidimensional, unstructured meshes made of arbitrary polyhedra.

The control volume technique used by Fluent stores value for all scalars at points located at the center of each control volume. However, the scalar values at cell faces are required for the convection terms in the discretized equations and must be interpolated from the cell center values. This is done using an upwind scheme, which means that the face value is derived from quantities in the cell upstream, or upwind, relative to the normal velocity direction. A second-order upwind scheme was chosen that uses a Taylor series expansion of the cell-centered solution about the cell centroid. The face value is found by

$$\phi_f = \phi + \nabla\phi \cdot \mathbf{r} \quad (4.8)$$

where ϕ is cell centered scalar value, f refers to the face value and \mathbf{r} is the displacement vector from the upstream cell centroid to face centroid.

4.4 Gradient Evaluation

Gradients and derivatives were calculated using the least squares cell based method. In this method, the solution is assumed to vary linearly between cell centers. The gradient between cells c_0 and c_1 along the vector $\delta\mathbf{r}_1$ from the centroid of cell c_0 to cell c_1 is given by equation (4.9):

$$(\nabla\phi)_{c0} \cdot \delta_{r1} = (\phi_{c1} - \phi_{c0}) \quad (4.9)$$

If similar equation are written for the remaining surrounding cells, a system of equations results that is overdetermined. The method solves the system of equations by decomposition using the Gram-Schmidt process [52].

4.5 Pressure Interpolation Scheme and Pressure-Velocity Coupling

The control volume technique used by Fluent stores all pressure data at points located at the center of each control volume. In order to express the cell face pressure values in terms of the cell center values, a second order pressure interpolation scheme was used. This scheme using a central differencing formula:

$$p_f = \frac{1}{2} (p_{c0} + p_{c1}) + \frac{1}{2} (\nabla p_{c0} \cdot \mathbf{r}_{c0} + \nabla p_{c1} \cdot \mathbf{r}_{c1}) \quad (4.10)$$

A pressure-velocity coupling scheme is required to derive an additional condition for pressure by reformatting the continuity equation. The ‘COUPLED’ algorithm was used. This algorithm solves the momentum and pressure-based continuity equations together. The full implicit coupling is achieved through an implicit discretization of pressure gradient terms in the momentum equations, and an implicit discretization of the face mass flux. A more detailed description of this method is available in the Fluent user’s manual [52].

4.6 Solution Solver

All simulations used the pressure-based solver with the coupled algorithm. The steps in this method include:

1. Update fluid properties
2. Simultaneously solve system of momentum and pressure-based continuity equations
3. Correct face mass fluxes
4. Check for solution convergence

The pressure based solver uses an algorithm called the projection method. In the projection method, the constraint of mass continuity on the velocity field is achieved by solving a pressure equation. The pressure equation is derived from the continuity and momentum equations so that the corrected velocity field satisfies the continuity equation. The governing equations are nonlinear and coupled to one another, so the solution process involves iterating the whole set of equations until the solution converges. The coupled algorithm was chosen over the segregated one because it results in faster solution convergence.

The pressure-based solver uses explicit under-relaxation parameters for momentum and pressure. The under-relaxation parameters reduce the change of a variable produced during each iteration. This control is necessary because of the nonlinearity of the equation set being solved. The new value of a variable in a cell is

$$\phi = \phi_{old} + \alpha\Delta\phi \quad (4.11)$$

where *old* refers to the value from the previous iteration and α is the under-relaxation factor. The value of these factors controls the speed with which a solution converges. The value of the under-relaxation parameters were varied for the different solutions and ranged from 0.5 to 0.75.

4.7 Computational Domain and Boundary Conditions

This study is concerned with the pressure drop in a generic block of foam. If the foam microstructure is modelled using the chosen idealized geometry model, a block would consist of hundreds of unit cells in each direction. Since the structure is repeating, it is reasonable to assume the flow in a generic section inside the foam is periodic in nature. Therefore, only a representative portion of the domain is required for the CFD model. Assuming the flow is steady, fully developed, and laminar with a unidirectional main stream in the x-direction, the computational domain can be reduced to a quarter of the geometric domain or unit cell without affecting the accuracy of the

results. This is the same approach used by previous numerical studies [20,18] that discretely modelled the microstructure of graphite foam. Figure 8 shows this computational domain.

The quarter unit-cells were modelled in CATIA V5 and imported into Ansys as IGS files for meshing. The fluid zone was meshed with tetrahedral control volumes. The body sizing tool in Ansys Meshing was used to control the cell size. 'Element size' was used as the control type and the meshing behavior was set to 'soft'. Default values were used for the growth rate, curvature normal angle and local minimum size. The element size was adjusted until the minimum control volume number determined by the grid independence study was reached.

The use of the streamwise periodic flow boundary condition between the inlet and outlet of the quarter unit-cell requires that the meshes on these surface be identical. The match control function in Ansys Meshing was used to produce identical meshes. The nodes on the outlet surface all have the same Y and Z coordinates as those on the inlet surface and are only translated in the X direction.

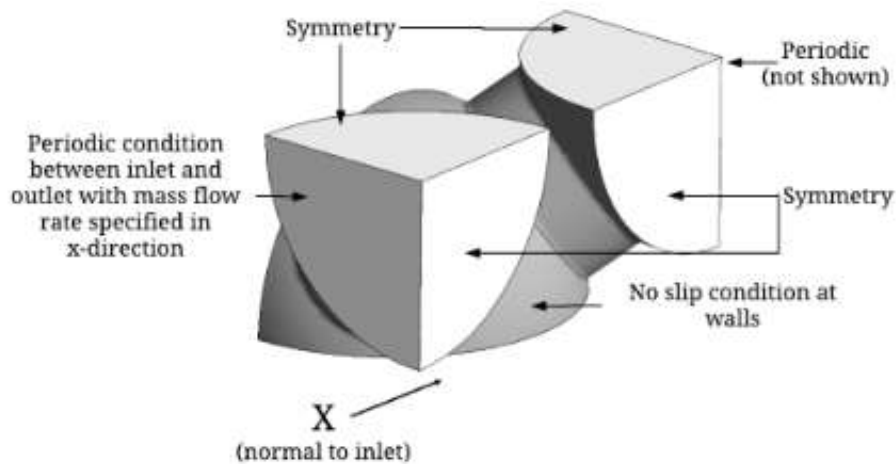


Figure 8. Computational domain and boundary conditions

The quality of each mesh produced was evaluated by checking the skewness, orthogonal quality, and the aspect ratio of all cells. The skewness of a cell varies from zero (good) to one (bad) and is the difference between the shape of the cell and the shape of an equilateral cell with the same volume. The orthogonal quality varies from one (good) to zero (bad) and is a measure of how orthogonal the faces of a cell are to the cell centroid. The aspect ratio is the measure of the stretching of a cell and is equal to the ratio of maximum to minimum cell dimensions. The maximum skewness for all cells was kept below 0.85, the minimum orthogonal quality was kept above 0.25, and the maximum aspect ratio was kept below 10 for all control volumes.

The following boundary conditions (shown in Figure 8) were applied for the CFD analysis:

- No slip at wall surfaces
- Symmetry on all external flat surfaces except inlet and outlet
- Mass flow at inlet of unit cell normal to face
- Streamwise periodic flow between inlet and outlet

The no slip boundary condition at the walls assumes zero fluid velocity ($\mathbf{u} = 0$). The symmetry boundary condition is valid since the unit volume can be thought of as repeating in space on all sides. Symmetry assumes the normal velocity and the normal pressure gradient are both zero at the symmetry plane.

Streamwise Periodic Flow

Several important concepts pertaining to periodic flows boundary conditions will be discussed. The Fluent theory guide [52] provides an overview of stream wise periodic boundary conditions. Periodicity implies the velocity vector repeats itself in space over some periodic length, L_p as follows:

$$\mathbf{u}(\mathbf{r}) = \mathbf{u}(\mathbf{r} + L_p) = \mathbf{u}(\mathbf{r} + 2L_p) = \dots \quad (4.12)$$

where \mathbf{r} is the position vector and \mathbf{L}_p is the periodic length vector. For viscous flows, the pressure is not periodic like the velocity. Rather, the pressure drop is periodic:

$$\Delta p = p(\mathbf{r}) - p(\mathbf{r} + \mathbf{L}_p) = p(\mathbf{r} + \mathbf{L}_p) - p(\mathbf{r} + 2\mathbf{L}_p) = \dots \quad (4.13)$$

When the pressure-based solver is used, the local pressure gradient is comprised of two parts: the gradient of a periodic component, $\nabla\tilde{p}(\mathbf{r})$, and the gradient of a linearly-varying component, $\sigma\mathbf{L}_p/|\mathbf{L}_p|$:

$$\Delta p(\mathbf{r}) = \nabla\tilde{p}(\mathbf{r}) + \sigma \frac{\mathbf{L}_p}{|\mathbf{L}_p|} \quad (4.14)$$

Because the value of σ is not known it must be iterated on until the specified mass flow rate is satisfied. An explicit under-relaxation factor is applied to the value of σ to control this convergence process. For all simulations in the present study, the gradient of a periodic component, $\nabla\tilde{p}(\mathbf{r})$ will be zero so the resulting value of σ will give the total pressure gradient.

4.8 Initial Conditions

The fluid used was air at 20°C, with a density of $\rho = 1.205 \text{ kg/m}^3$ and a dynamic viscosity, $\mu = 1.821 \times 10^{-5} \text{ Pa} \cdot \text{s}$ [53]. The pressure and velocity were initialized using Fluent's hybrid initialization tool, which is a collection of recipes and boundary interpolation methods. The initial velocity profile is produced by solving Laplace's equation with the appropriate boundary conditions.

$$\nabla^2 \varphi = 0 \quad (4.15)$$

where φ is the velocity potential. The velocity components are given by the gradient of the potential.

$$\mathbf{u} = \nabla\varphi \quad (4.16)$$

The velocity potential at boundaries depends on the boundary condition:

- Wall and symmetry boundaries: the velocity normal to the wall is zero.

$$\left. \frac{\partial \varphi}{\partial n} \right|_{wall} = 0 \quad (4.17)$$

- Periodic boundaries: the velocity normal to the inlet are computed from the user-input values.

$$\left. \frac{\partial \varphi}{\partial n} \right|_{inlet} = u_{\perp} \quad (4.18)$$

The pressure field was initialized as the averaged constant value of all the boundaries, which is the same as the specified operating pressure (1 atm for all cases).

4.9 Stability and Convergence

Each simulation was considered converged when the residuals for x, y and z momentum and continuity were below 10^{-6} . The residuals were monitored during each simulations to ensure that the solution was stable. In addition, the value of σ , or the pressure gradient used in the periodic boundary condition was monitored to ensure that the value was stable and had converged when the residuals reached the target for convergence.

4.10 Grid Independence Study

A grid independence study was performed to ensure the results of the numerical simulations were independent of the mesh sizing. The study was performed on a single model and the ratio of the number of cells to the hydraulic diameter was used for all models in future simulations. The model used for the study was sample 2A with a porosity of 0.75 and the highest flow rate considered. For each simulation, the number of cells was adjusted. After the solutions converged and it was determined that the solution was stable, the pressure drop was recorded. Then the number of cells was increased by a factor of approximately 1.5 and the process was repeated.

The solutions was determined to be independent of the mesh size when the pressure drop was changing by less than 0.05% between consecutive trials. In order to ensure grid independence for models with different dimensions and length scales, a variable called the mesh ratio, n , was defined as the ratio of the number of cells in the mesh to the hydraulic radius of the model as defined in equation (2.15).

$$n = \frac{N}{D_h} = \frac{N\beta}{4\epsilon} \quad (4.19)$$

As seen in Table 6 and Figure 9, the results are independent of the mesh sizing when the mesh ratio is equal to 235. All models will use a minimum mesh ratio of $n = 235$ for all simulations. The minimum number of cells required to maintain this minimum mesh ratio for each model, as well as the actual number of elements used in each model are shown in Table 7.

Table 6. Grid Independence Study Results

Number of Cells, N (x1000)	Mesh Ratio, N/D_h (1/μm)	Pressure Gradient (kPa/m)	Change in Pressure Gradient (%)
8.18	24.84	200.20	n/a – baseline
14.23	43.22	201.82	0.81
21.65	65.76	202.64	0.41
31.86	96.77	202.97	0.16
47.32	143.74	204.77	0.89
61.35	186.36	204.66	-0.05
77.47	235.33	204.71	0.02

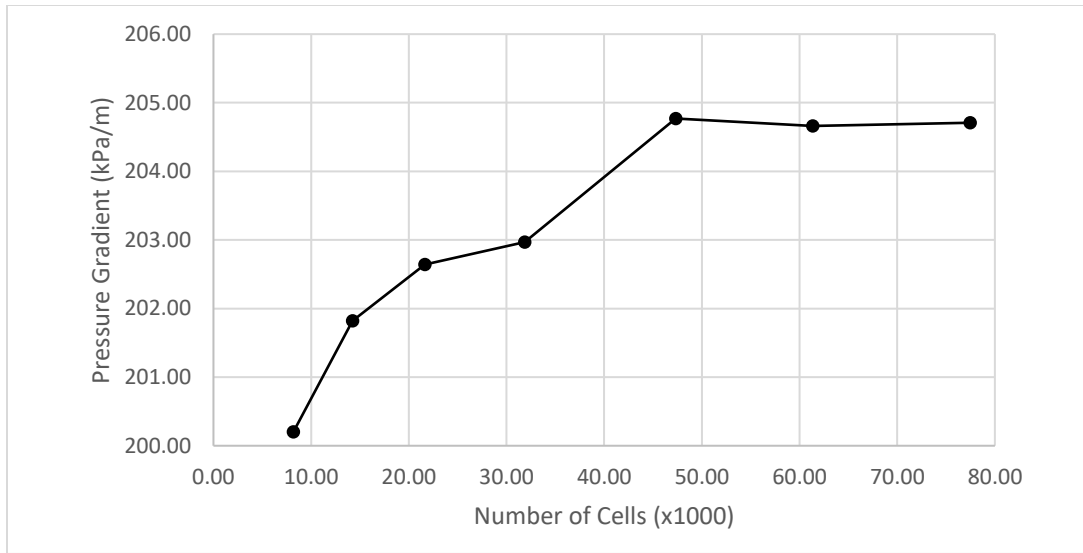


Figure 9. Grid independence study results using model 2A with 0.75 porosity

Table 7. Minimum number of cells required for each model to satisfy the mesh ratio requirement ($n=235$) from the grid independence study and the actual number of cells used in each model.

Model	Porosity	Minimum Number of Cells Required	Number of Cells Used in Model
2A	0.75	77,362	79,119
	0.85	85,120	88,354
3A	0.75	109,913	134,377
	0.85	120,856	125,435
3B	0.75	185,519	192,336
	0.85	233,951	242,982
3C	0.75	119,985	123,240
	0.85	147,556	158,401
4A	0.75	200,449	210,385
	0.82	208,440	215,467
4B	0.75	243,537	258,468
	0.85	305,086	322,908
4C	0.75	280,306	306,164
	0.85	321,584	325,575
U1	0.75	196,845	213,107
	0.85	229,337	259,715
U2	0.75	244,616	279,668
	0.85	274,212	290,267

4.11 Summary of Simulation Parameters

A summary of the various parameters used in the solution for each model is shown in Table

8.

Table 8. Summary of various parameters used for numerical simulations in Fluent.

Model	Geometry			Mesh		Under-relaxation Factors			
	Porosity	D _p (μm)	D _w (μm)	t (μm)	Element Size ($\times 10^{-5}$)	Number of Cells	Pressure	Momentum	β
2A	0.75	342	157	35	1.1	79,119	0.5-0.75	0.5-0.75	0.5
	0.85			8	1.03	88,354			
3A	0.75	491	222	43	1.3	134,377			
	0.80			27	1.3	130,555			
	0.85			12	1.3	125,434			
3B	0.75	633	372	159	1.6	192,336			
	0.85			96	1.3	242,982			
3C	0.75	405	293	227	1.5	123,240			
	0.85			171	1.2	158,401			
4A	0.75	1004	360	35	2.4	210,385			
	0.82			0	2.3	215,467			
4B	0.75	849	522	258	2.0	258,468			
	0.85			167	1.75	322,908			
4C	0.75	1159	612	189	2.4	306,164			
	0.80			139	2.25	311,030			
	0.85			94	2.25	325,575			
U1	0.75	800	444	159	1.9	213,107			
	0.80			122	1.8	234,786			
	0.85			87	1.7	259,715			
U2	0.75	1050	512	125	2.2	279,668			
	0.80			85	2.2	265,698			
	0.85			50	2.1	290,267			

CHAPTER 5

PREPARATION OF EXPERIMENTAL DATA

The results of the numerical simulations will be validated using the experimental results for pressure drop from Thompson [15]. In order for the numerical results to be compared directly to the experimental results, the experimental results must be transformed into the appropriate form. The experimental results for pressure drop are presents in a graph of Reynolds number versus pressure drop as shown in Figure 10. The values for Reynolds number and pressure drop were extracted from the electronic form of the graph using the free software XYScan. Not all specimens shown in Figure 10 have reported values for pore diameter and window diameter. Data was extracted only for the specimens with reported values for pore and window diameter.

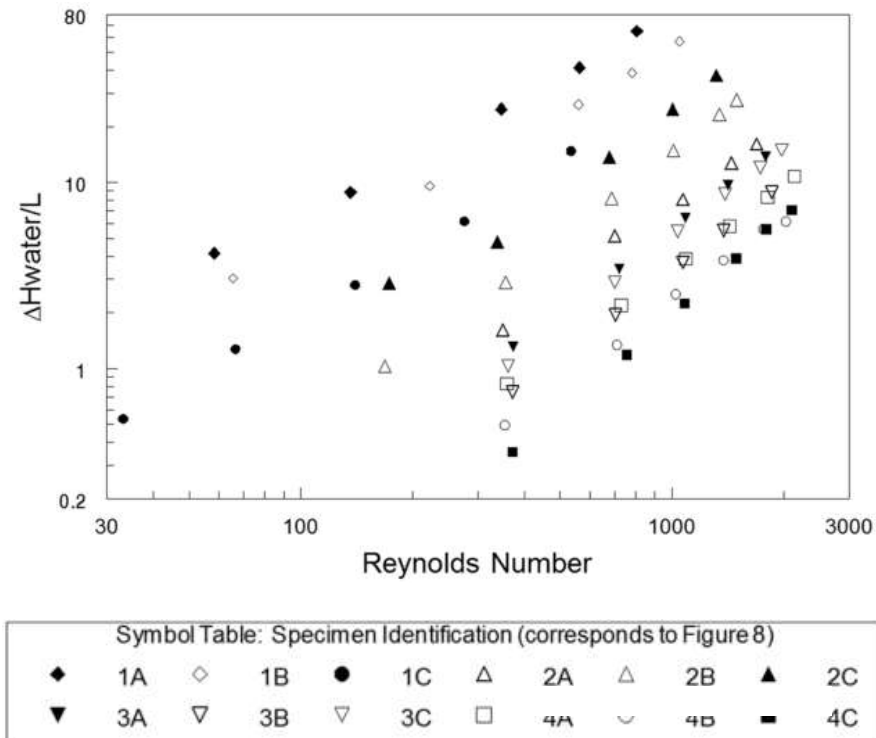


Figure 10. Experimental pressure drop in water column change per length as a function of Reynolds number reported by Thompson [15] used to validate numerical results of the present study.

The length scale used in the Reynolds number calculation for the experimental data is the hydraulic radius of the channel:

$$D_{h,exp} = \frac{4 \cdot area}{perimeter} = \frac{4WH}{2(W + H)} \quad (5.1)$$

where W and H are the width and height of the channel and are equal to 25.4 mm and 6 mm, respectively, in the experiment. The bulk fluid velocity is used in the experimental Reynolds number calculation.

$$Re_{exp} = \frac{\rho U D_{h,exp}}{\mu} \quad (5.2)$$

The experimental Reynolds numbers are converted to bulk fluid velocity values for comparison to the numerical results using the following equation:

$$U = \frac{Re_{exp} \mu}{\rho D_{h,exp}} \quad (5.3)$$

where the properties of air at 20°C are $\rho = 1.205 \text{ kg/m}^3$ and $\mu = 1.821 \times 10^{-5} \text{ Pa} \cdot \text{s}$ [53].

The pressure drop data in the experiment was reported in units of water column change per unit length, or $\Delta H_{water}/L$. These numbers were converted to kPa/m for comparison to numerical results using

$$\Delta P_{kPa/m} = \frac{\Delta H_{water}}{L} \cdot \frac{\rho_{water} g}{1000} \quad (5.4)$$

where the density of water at 20°C is $\rho_{water} = 998.3 \text{ kg/m}^3$ [53] and the acceleration due to gravity is $g = 9.81 \text{ m/s}^2$.

The extracted pressure drop data for the appropriate specimens as well as the transformed data (using equations (2.5) and (2.6)) are shown in Table 9.

Table 9. Experimental pressure drop data reported by Thompson [15] and transformed for use in validating numerical results.

Sample	Reported				Transformed	
	Pore Diameter (μm)	Window Diameter (μm)	Re,exp	$\Delta H_{\text{water}}/L$	U (m/s)	$\Delta P/L$ (kPa/m)
2A	342	157	350.18	1.58	0.55	15.46
			702.30	5.06	1.09	49.59
			1069.94	7.97	1.67	78.1
			1445.30	12.56	2.25	123.01
			1687.02	15.83	2.63	155.04
3A	491	222	373.48	1.33	0.58	13.02
			720.64	3.50	1.12	34.3
			1088.49	6.60	1.69	64.68
			1414.58	9.88	2.2	96.77
			1791.60	14.04	2.79	137.51
3B	633	372	371.88	0.76	0.58	7.46
			705.33	1.99	1.1	19.48
			1069.94	3.82	1.67	37.37
			1378.59	5.61	2.15	54.96
			1854.24	9.07	2.89	88.82
4A	1004	360	360.87	0.83	0.56	8.13
			729.99	2.19	1.14	21.41
			1093.17	3.92	1.7	38.34
			1426.79	5.81	2.22	56.87
			1814.84	8.32	2.82	81.52
			2136.65	10.86	3.33	106.33
4B	849	522	354.72	0.50	0.55	4.86
			711.41	1.34	1.11	13.13
			1024.95	2.51	1.6	24.55
			1378.59	3.82	2.15	37.37
			1753.53	5.66	2.73	55.43
			2029.29	6.17	3.16	60.39
4C	1159	612	371.88	0.36	0.58	3.51
			755.51	1.19	1.18	11.65
			1083.82	2.24	1.69	21.96
			1489.42	3.92	2.32	38.34
			1799.31	5.61	2.8	54.96
			2100.25	7.13	3.27	69.87

CHAPTER 6

RESULTS AND ANALYSIS

Numerical simulations were ran for all the models listed in Table 8. This includes models matching the pore and window diameter of the samples used in the Thompson experiment [15] as well as user-defined models. At least two models were ran for each unique value of pore diameter and window diameter, one with a porosity matching the lowest value in the reported range (0.75) and another matching the highest value (0.85). The exception to this is the higher porosity model for sample 4A which has a porosity of 0.82, since this is the highest porosity allowed with the given pore and window diameter for the idealized model (window thickness is zero). Additional user-defined models were included in the numerical simulations so that more data points could be used in the pressure drop correlation development. The user-defined samples (U1 and U2) have values of D_p/D_w and D_h that are different than the other models and fill in the gaps in these values between the values for the other models.

As mentioned in section 3.3, the expressions for the idealized geometry model are limited to cases where the ratio D_p/D_w is greater than 1.73. Three samples used in the Thompson experiment do not meet this requirement. Samples 3B, 3C and 4B have respective D_p/D_w values of 1.70, 1.38 and 1.63. In these cases the cylinders representing the inter-pore windows intersect one another. As seen in Figure 11, this effect is minor for D_p/D_w values close to 1.73 (samples 3B and 4B), but more significant for lower values like 1.38 (sample 3B). For this reason, models were not run for sample 3C. In an effort to maximize the number of models for which direct comparisons to the experimental data could be performed, models for samples 3B and 4B were included. The validity of this decision will be discussed later.

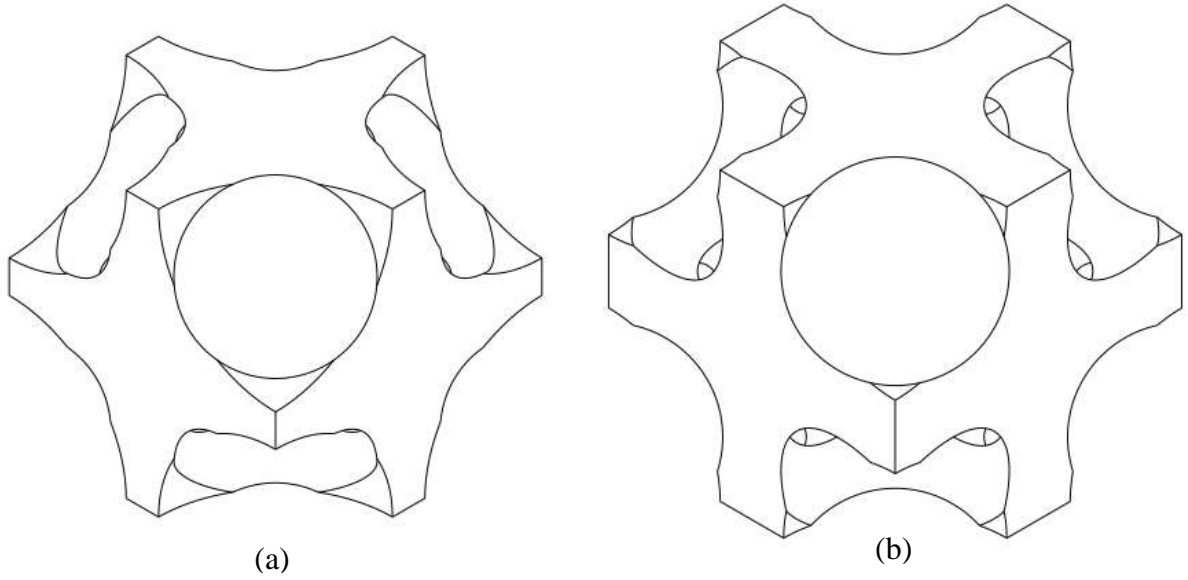


Figure 11. Models with D_p/D_w values below 1.73 where the windows intersect each other, (a) 4B with $D_p/D_w=1.63$ and (b) 3C with $D_p/D_w=1.38$.

The mass flow rate for each model was varied so that the Reynolds number, given by equation (2.17) ranges from 0 to 300, which is considered the cutoff for laminar flow (see section 2.6.7). Reynolds numbers close to zero were included in order to observe the transition from linear or Darcy flow to inertial flow. The numerical results for each sample are in Table 15 in appendix A.

It is convenient to transform the numerical results so that they are in dimensionless form. Starting with the Darcy-Forchheimer equation, the normalized pressure drop used by Karimian [18] is defined as

$$\Pi_D = - \left(\frac{\Delta P}{L} \right) \left(\frac{D_h^2}{\mu U} \right) \quad (6.1)$$

and the normalized permeability is

$$K_D = \frac{K}{D_h^2} \quad (6.2)$$

Using equations (6.4) and (6.5) the Darcy-Forchheimer equation can be written in dimensionless form as

$$\Pi_D = \frac{1}{K_D} + \frac{c_F}{\sqrt{K_D}} Re_h \quad (6.3)$$

where Re_h is the Reynolds number based on the hydraulic radius given by equation (2.17). A plot of normalized pressure drop as a function of Reynolds number for all simulations is shown in Figure 12.

Three distinct flow regimes can be seen from the results in Figure 12: Darcy or creeping flow, transition to inertial flow, and inertial flow. For Reynolds number approximately below five, the normalized pressure drop is a constant, indicating the form coefficient, c_F , in equation (6.3) is zero. Viscous forces dominate over inertial forces in this region. In the region $15 < Re_h < 300$ the behavior of the curves in Figure 12 (a) is linear with a non-zero slope. This indicates both terms on the right hand side of equation (6.3) are significant and both the viscous and inertial forces contribute to pressure drop. The influence of the inertial forces continues to increase as fluid velocity increases and the pressure gradient varies with the square of fluid velocity. In the transition region, $5 < Re_h < 15$, the curves in Figure 12 (c) are neither a constant value or linear with a constant slope. The data shows curvature indicating contribution from terms that are higher than second order, or quadratic, with respect to velocity. The behavior in this region is in fact cubic with respect to velocity, or quadratic with respect to Reynolds number. This so-called “weak inertial” region was observed in previous numerical studies by Karimian [18] and is in agreement with the findings of Mei and Auriault [55] for flow through porous media. The results for $Re_h < 15$ were included in the numerical simulations so that a cutoff value could be determined for the inertial flow region that is the focus of the current study. The pressure drop correlations will focus on the inertial range, or $15 < Re_h < 300$.

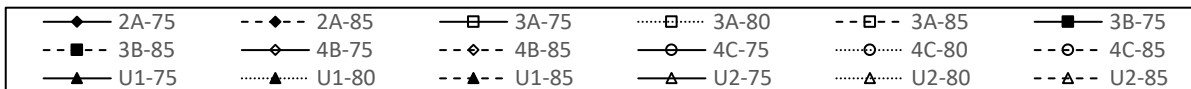
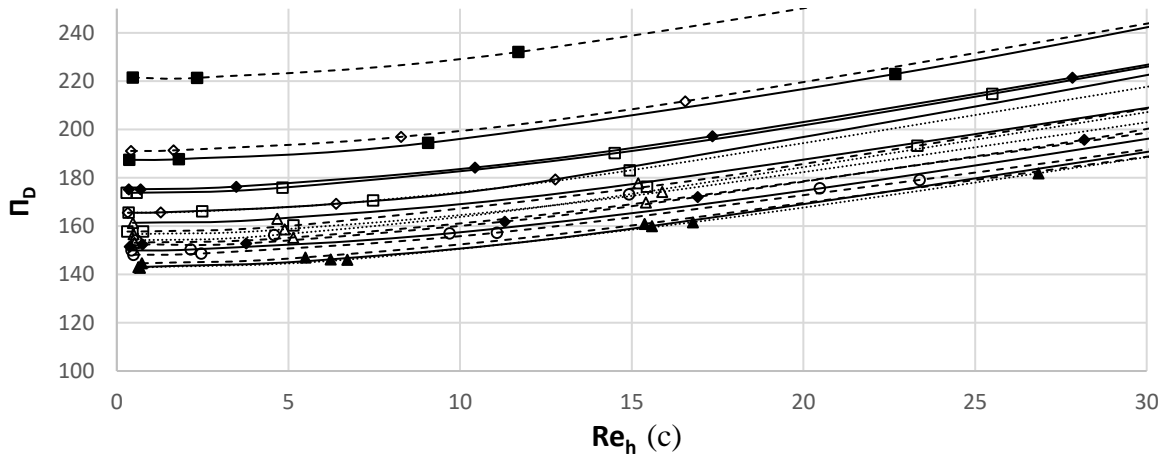
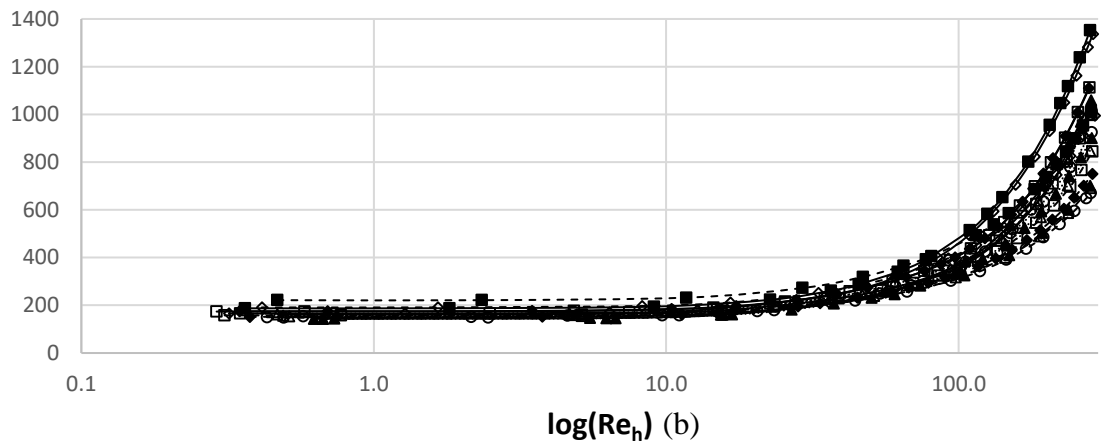
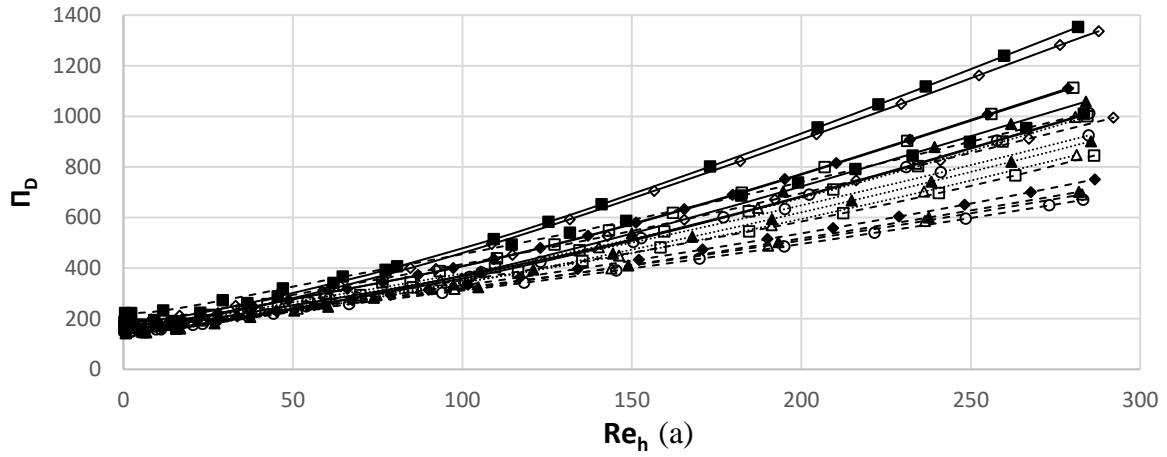


Figure 3. Normalized pressure drop versus pore level Reynolds number from the numerical simulations. (a) Standard scale, (b) $\log_{10}(\text{Re}_h)$ scale to show Darcy flow region, and (c) standard scale for $0 < \text{Re}_h < 30$ to show transition from Darcy to inertial flow.

6.1 Model Validation

Before pressure drop expressions can be developed using the results of the numerical simulations, the results must be validated by comparing them to the experimental results from Thompson. The purpose of the simulations is to develop correlations for the permeability and inertial coefficient. Therefore, the simulation results are considered valid if the predicted values of the coefficients produced using the simulation results is within the range of uncertainty of the values of the coefficients produced from the experimental data. The experimental results are presented in pressure gradient as a function of fluid velocity. For the purpose of validation, only the numerical results for fluid velocity within the limits of experimental data will be used for comparison. Plots of pressure gradient versus fluid velocity for both the experimental and numerical results for each model are in appendix B.

Working with the non-dimensional form of the momentum equation presented earlier simplifies the calculations for the permeability and form coefficient to involve simple linear regression. However, a problem arises when using the normalized pressure drop with the experimental data presented by Thompson. The paper reports porosity ranges for the samples tested, but not precise numbers. Therefore, the hydraulic diameter of the pore samples cannot be computed and the experimental pressure curves cannot be normalized using equation (6.6). For purposes of validating the numerical results by direct comparison with experimental results, the momentum equation will be linearized in a different way. The pressure drop expression in equation (2.10) can be linearized by introducing the following variables:

$$x = \frac{\rho U}{\mu} \quad (6.4)$$

$$y = -\frac{\Delta p}{L} \frac{1}{\mu U} \quad (6.5)$$

Using the x and y variables equation (2.10) becomes.

$$y = \frac{1}{K} + \frac{c_F}{K^{\frac{1}{2}}}x \quad (6.6)$$

This is the equation of a line where the permeability can be calculated from the intercept and the form coefficient can be calculated from the slope. The experimental results from Thompson as well as the numerical results of the present study were transformed using the expression for x and y . Simple least-squares linear regression analysis following the method from Navidi [54] was performed with both the numerical and experimental data to find the intercept and slope values with a 95% confidence interval. The value of the coefficients of a least-squares line given by $\hat{y} = \hat{b}_0 + \hat{b}_1x$ and fitting data points $(x_1, y_1) \dots, (x_n, y_n)$ are [54]

$$\hat{b}_1 = \frac{\sum_{i=1}^n (x_i - \bar{x})(y_i - \bar{y})}{\sum_{i=1}^n (x_i - \bar{x})^2} \quad (6.7)$$

$$\hat{b}_0 = \bar{y} - \hat{b}_1\bar{x} \quad (6.8)$$

The standard deviation in the least-squares coefficients can be calculated if it is assumed that the errors associated with each data point are random and independent, have a mean of zero, have the same variance, and are normally distributed. In the equations that follow s is the standard error and r is the correlation coefficient [54].

$$s_{\hat{b}_1} = \frac{s}{\sqrt{\sum_{i=1}^n (x_i - \bar{x})^2}} \quad (6.9)$$

$$s_{\hat{b}_0} = s \sqrt{\frac{1}{n} + \frac{\bar{x}^2}{\sum_{i=1}^n (x_i - \bar{x})^2}} \quad (6.10)$$

$$\text{where } s = \sqrt{\frac{(1-r^2) \sum_{i=1}^n (y_i - \bar{y})^2}{n-2}} \quad (6.11)$$

$$\text{and } r^2 = \frac{\sum_{i=1}^n (y_i - \bar{y})^2 - \frac{(\sum_{i=1}^n (y_i - \bar{y}))^2}{n}}{\sum_{i=1}^n (y_i - \bar{y})^2} \quad (6.12)$$

Confidence intervals of level $100(1 - \alpha)\%$ for these coefficients are [54]

$$\hat{b}_1 \pm t_{n-2, \alpha/2} \cdot s_{\hat{b}_1} \quad (6.13)$$

$$\hat{b}_0 \pm t_{n-2, \alpha/2} \cdot s_{\hat{b}_0} \quad (6.14)$$

Where $t_{n-2, \alpha/2}$ denotes the point on the student's t distribution curve with $n - 2$ degrees of freedom that cuts off an area of $\alpha/2$ in the right hand tail. Equations (4.4) through (6.14) were used to calculate the least-squares coefficients along with their 95% confidence intervals for the experimental data as well as for each numerical model.

The statistical significance of the coefficients was checked by computing the P-value for the tests of the hypotheses that the coefficients are equal to zero. The P-value is the probability that the coefficient is zero. To test the hypothesis that a coefficient, \hat{b} is zero, first the z-value is computed as

$$z = \frac{\hat{b}}{s_{\hat{b}}/\sqrt{n}} \quad (6.15)$$

The P-value is then the area under the normal distribution curve in the tails cut off by z and $-z$. The P-value for all coefficient was below 0.05, meaning that it can be said that the coefficients are not equal to zero with a statistical significance level of 95% or higher.

The paper from the Thompson experiment did not report the uncertainty in each data point. By using the uncertainty in the least-squares coefficients, the uncertainty in the experimental data is able to be captured without knowledge of the uncertainty in each data point. Assuming the experimental errors are random, independent, and normally distributed, the uncertainty in the least-squares coefficients will capture the effect of these errors. The results of the least square regression analysis for both the experimental and numerical results are shown in Table 10 and Figure 13.

Table 10. Least-squares curve fit coefficient values with 95% confidence intervals resulting from fitting the experimental and numerical results to equation (4.3).

Sample	Experimental		Numerical, $\varepsilon = 0.75$		Numerical, $\varepsilon = 0.85$	
	Intercept ($1/m^2 \times 10^{-9}$)	Slope ($1/m$)	Intercept ($1/m^2 \times 10^{-9}$)	Slope ($1/m$)	Intercept ($1/m^2 \times 10^{-9}$)	Slope ($1/m$)
2A	1.38 ± 0.76	0.11 ± 0.06	1.39 ± 0.03	0.11 ± 0.002	1.08 ± 0.04	0.07 ± 0.003
3A	0.90 ± 0.22	0.10 ± 0.02	0.65 ± 0.06	0.08 ± 0.005	0.56 ± 0.02	0.05 ± 0.002
3B	0.50 ± 0.10	0.06 ± 0.01	0.12 ± 0.08	0.08 ± 0.006	0.17 ± 0.02	0.04 ± 0.002
4A	0.63 ± 0.06	0.05 ± 0.004	0.16 ± 0.02	0.12 ± 0.001	-0.08 ± 0.08	0.15 ± 0.008
4B	0.34 ± 0.10	0.04 ± 0.01	0.05 ± 0.04	0.07 ± 0.004	0.07 ± 0.03	0.03 ± 0.002
4C	0.15 ± 0.05	0.05 ± 0.01	0.06 ± 0.04	0.04 ± 0.005	0.07 ± 0.02	0.02 ± 0.002

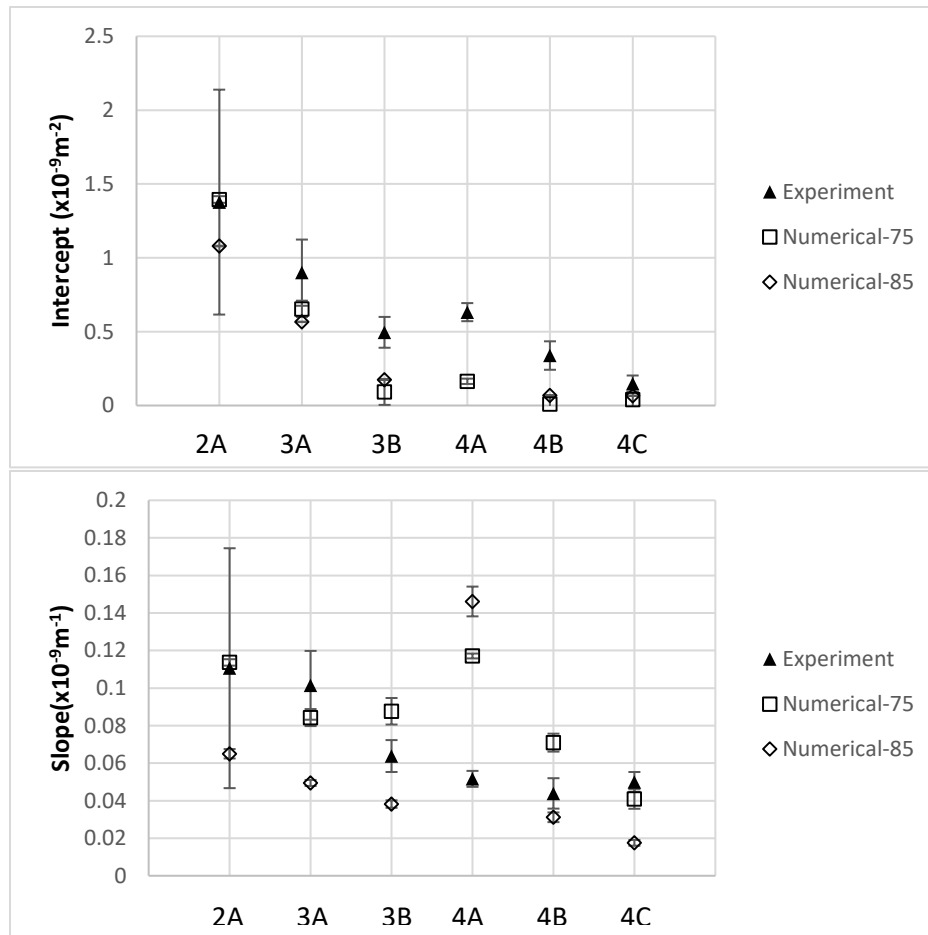


Figure 13. Least-squares curve fit coefficient values with 95% confidence interval error bars resulting from fitting the experimental and numerical results to equation (4.3).

In order for the experimental results to validate the numerical results, the range of values for the coefficients in Table 10 and Figure 13 predicted by the numerical results must fall within the range of uncertainty of the values predicted by the experimental results. Since the experimental data reported a range of porosity between 0.75 and 0.85, this means that the range of uncertainty in the coefficients from the experimental data must intersect the range of values between the coefficients for the 0.75 and 0.85 porosity models. Using this approach and the values in Table 10 and Figure 13 it can be seen that the predicted values for the intercept coefficients from the numerical results are validated for samples 2A, 3A and 4C. The range of values for the numerical results intersect the error bars for the experimental results. Likewise, the predicted values for the slope coefficients are validated for samples 2A, 3A, 3B, 4B and 4C.

Using the curve-fit coefficients method, the models for samples 2A, 3A, 3B, 4B and 4C are valid for predicting the slope in equation (4.3). However, only models for 2A, 3A, and 4C are valid for predicting the intercept coefficient. The predicted values of the intercept for models 3B and 4B can be validated by comparing the curves for pressure gradient as a function of fluid velocity for the numerical and experimental results shown in Figure 14 and Figure 15.

As seen in Figure 14 and Figure 15, the numerical results for a porosity of 0.75 are close to the experimental numbers. The quadratic term in the numerical results is more dominant than in the experimental results, creating a sharper curve. This is why the intercept from the numerical results, which represents the linear contribution to the curve, is lower than the intercept from the experimental results. However, regardless of the shape of the curve, the numerical results for samples 3A and 4A agree reasonably well with the experimental data. Therefore, the models for sample 3A and 4A are also valid at predicting the intercept coefficient since the net result is a pressure drop prediction that agrees with experimental results.

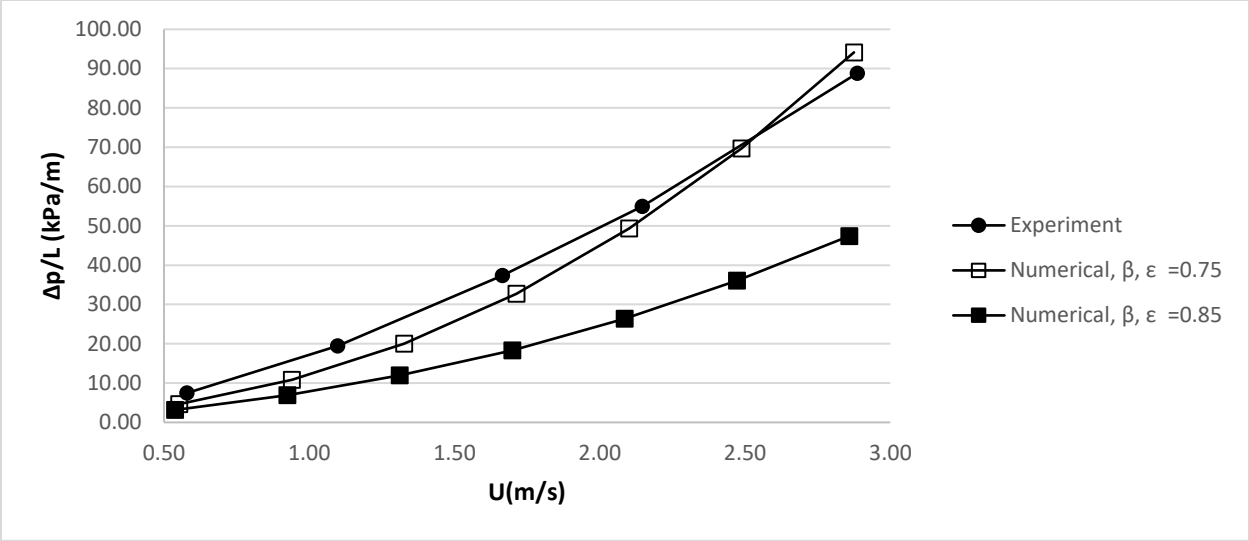


Figure 14. Numerical and experimental results for pressure gradient as a function of fluid velocity for sample 3B.

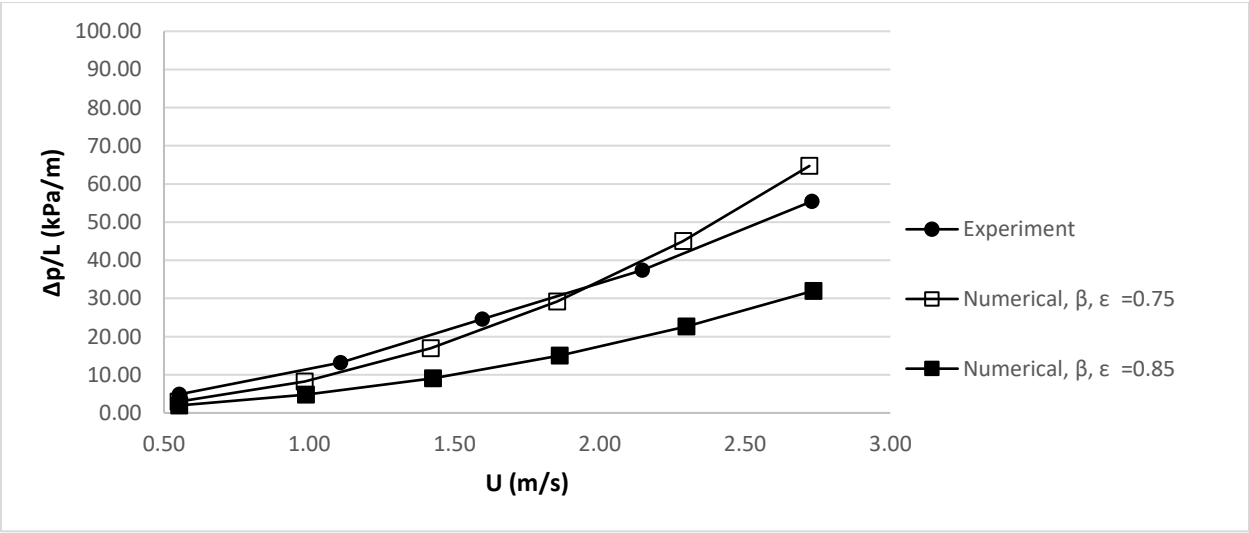


Figure 15. Numerical and experimental results for pressure gradient as a function of fluid velocity for sample 4B.

The numerical results from models for samples 2A, 3A, 3B, 4B and 4C were validated using experimental data, while the results from the models for samples 4A did not agree with experimental results and could not be validated. A possible explanation for the ability of the

numerical simulations to validate some models but not all can be found by examining the ratio of the pore diameter to window diameter for each sample shown in Table 11.

Table 11. Ratio of pore diameter to window diameter of various models and its effect on the validity of the numerical simulations.

Sample	D_p (μm)	D_w (μm)	D_p / D_w	Validated / Not Validated
2A	342	157	2.18	Validated
3A	491	222	2.22	Validated
3B	633	372	1.70	Validated
3C	405	293	1.38	Not Validated
4A	1004	360	2.79	Not Validated
4B	849	522	1.63	Validated
4C	1159	612	1.89	Validated

As seen in Table 11, the two models that were not validated have pore diameter to window diameter ratios (D_p/D_w) that are outside of the range of the values for the models that were successfully validated. The ratio for sample 3C (1.38) is below the next lowest value for a sample that was validated (1.63 for sample 4B). As mentioned earlier, sample 3C was not included in the simulations because of its low D_p/D_w value. Likewise, the ratio for sample 4A is above the next highest value for a sample that was validated (2.22 for sample 3A). Therefore the numerical simulations are only valid with the range of D_p/D_w ratios covered by the validated models, which is between 1.63 and 2.22.

Further insight into the failure to validate models for sample 4A can be gained by looking at the curves for pressure gradient as a function of fluid velocity for this sample shown in Figure 16.

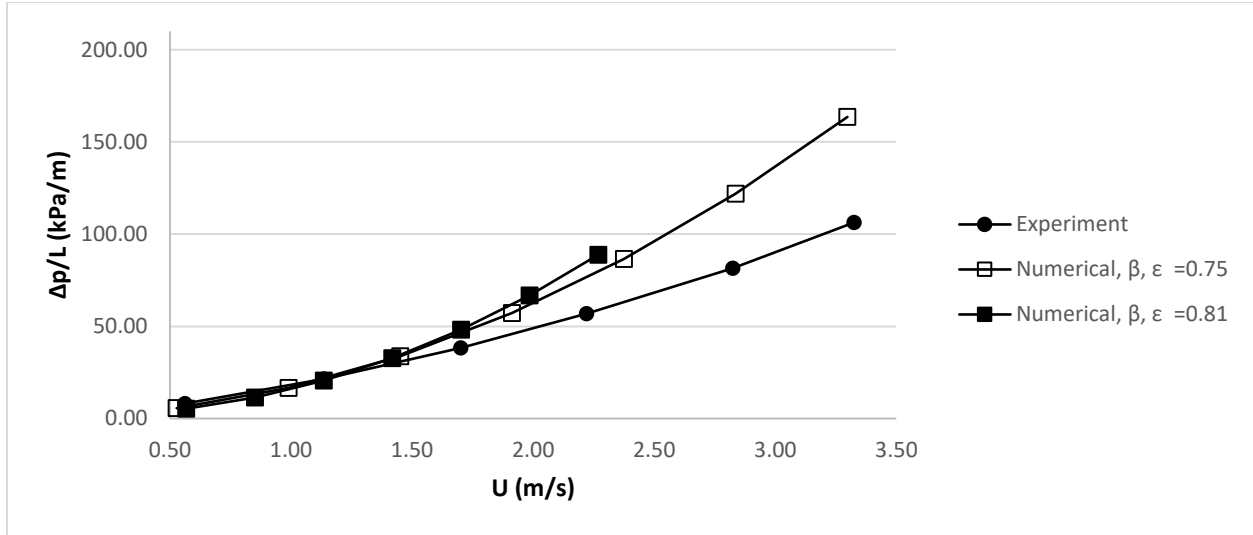


Figure 16. Numerical and experimental results for pressure gradient as a function of fluid velocity for sample 4A.

The numerical results for pressure gradient for sample 4A shown in Figure 16 quickly divert from the experimental values at high fluid velocities. This indicates that the numerical model is over-estimating the inertial effects on pressure drop, which cause the quadratic behavior of the pressure gradient curve. As discussed in section 2.6.2, these inertial effects are caused by the pressure drop across a blunt body in a fluid stream. If the “blunt body” is considered to be the solid portion of the matrix that causes the fluid to contract through the inter-pore windows, the effect of this body on pressure drop would increase as the ratio of D_p/D_w increases. This effect is also analogous to pressure loss associated with a sudden expansion or contraction in a pipe or through an orifice, where the pressure drop is proportional the square of fluid velocity and increases as the ratio of the pipe diameters, D_{large}/D_{small} , increases [56]. At the high D_p/D_w ratio used for sample 4A, the numerical model is over-estimating these inertial effects and is not valid.

6.2 Pressure Drop Correlations

The numerical models were validated for Reynolds numbers (as defined in equation (2.17)) from 15-300 and for D_p/D_w ratios between 1.63 and 2.22. Now that a valid range has been established for which the predictions of the numerical models match the experimental data, correlations for the permeability and inertia coefficient can be developed within this range. The goal of this section is to use the numerical results to develop correlations for the permeability and inertia coefficient as a function of foam microstructure, specifically the pore diameter, inter-pore window diameter and the porosity. The permeability and form coefficient of each model were found by least-squares curve fitting of the data in Figure 12 for Reynolds numbers between 15 and 300. If b_0 and b_1 are the intercept and slope coefficients from the curve fit, then the permeability and form coefficient are

$$K = \frac{D_h^2}{b_0} \quad (6.16)$$

$$c_F = b_1 \sqrt{b_0} \quad (6.17)$$

If the 95% confidence intervals for the coefficients are $\pm e_{b_0}$ and $\pm e_{b_1}$, then the same confidence intervals for K and c_F are [57]

$$e_K = \frac{e_{b_0}}{b_0} K \quad (6.18)$$

$$e_{c_F} = \sqrt{\left(\frac{e_{b_0}}{2b_0}\right)^2 + \left(\frac{e_{b_1}}{b_1}\right)^2} c_F \quad (6.19)$$

The results for the values of the permeability and form coefficient calculated from the numerical results and used for the proceeding expressions are in Table 12.

Table 12. Permeability and form coefficient values with 95% confidence interval error values calculated from the least-squares regression analysis of the numerical results.

Model	Porosity ϵ	K (10^{-9} m^2)	$e_{K,95\%}$	C_F	$e_{C_F,95\%}$
2A	0.75	1.24	0.42	0.37	0.07
	0.85	1.01	0.07	0.18	0.01
3A	0.75	2.44	0.98	0.37	0.08
	0.80	2.41	0.94	0.30	0.06
	0.85	2.14	0.32	0.22	0.03
3B	0.75	8.88	4.64	0.52	0.14
	0.85	5.76	0.52	0.22	0.02
4B	0.75	18.43	12.64	0.57	0.20
	0.85	11.60	1.52	0.23	0.03
4C	0.75	20.37	10.84	0.38	0.10
	0.80	15.26	5.95	0.27	0.06
	0.85	14.65	1.25	0.17	0.01
U1	0.75	10.64	7.18	0.42	0.14
	0.80	9.38	2.81	0.30	0.05
	0.85	7.88	1.20	0.18	0.02
U2	0.75	11.92	8.70	0.32	0.12
	0.80	11.16	4.83	0.24	0.06
	0.85	10.16	1.44	0.17	0.02

6.2.1 Permeability Model

The permeability of a matrix is a measure of the effect of viscous shear stresses imposed by the solid matrix on the fluid. In order to propose a possible form of the expression for the permeability of graphite foam, pressure losses in pipe flow will be briefly discussed. For laminar flow through a pipe, the pressure gradient is [53]

$$\frac{\Delta P}{L} = \frac{A\mu U}{D^2} \quad (6.20)$$

where U is the average fluid velocity, D is the hydraulic diameter of the pipe, and A is a constant that depends on the pipe cross section ($A=32$ for circular pipe). For the case of flow through porous media with no inertial effects, the pressure gradient is

$$\frac{\Delta P}{L} = \frac{\mu U}{K} \quad (6.21)$$

Comparing equations (6.20) and (6.21), it is reasonable to expect the permeability to be proportional to the square of the hydraulic radius over some constant, or

$$K \propto \frac{D_h^2}{A} \quad (6.22)$$

The plot in Figure 17 shows the square of the hydraulic radius in equation (2.15) versus the permeability calculated from the numerical results. The plot shows a strong dependence of the permeability on D_h^2 , but there is also a dependence on the porosity. This suggests that the constant A in equation (6.22) is some function of porosity. If this constant is ε^n where n is an integer, n can be iterated on until the curves in Figure 17 lie on top of one another.

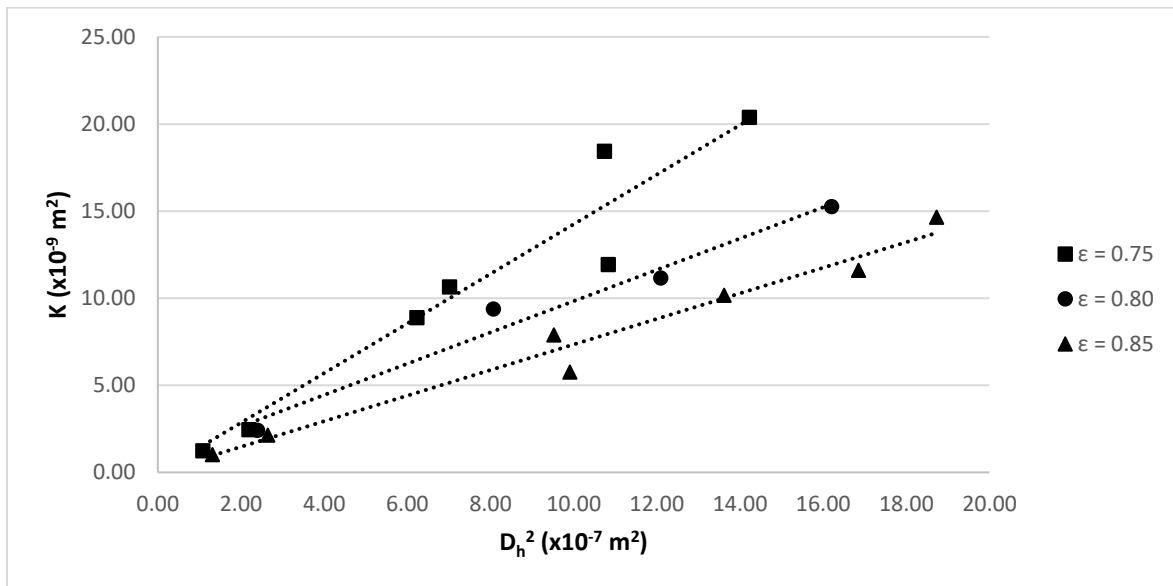


Figure 17. Plot of the permeability calculated using the numerical results as a function of the square of the hydraulic radius.

Assuming the constant A is ε^n , n was iterated until a linear fit of all the data points with the maximum correlation was found. The maximum correlation results when $n = 5.4$ and the curve

shown in Figure 18 results. Error bars representing 95% confidence intervals for the least-squares coefficients are shown. When $\varepsilon^{5.4}$ is introduced, the linear curves for each porosity lie on top of each other.

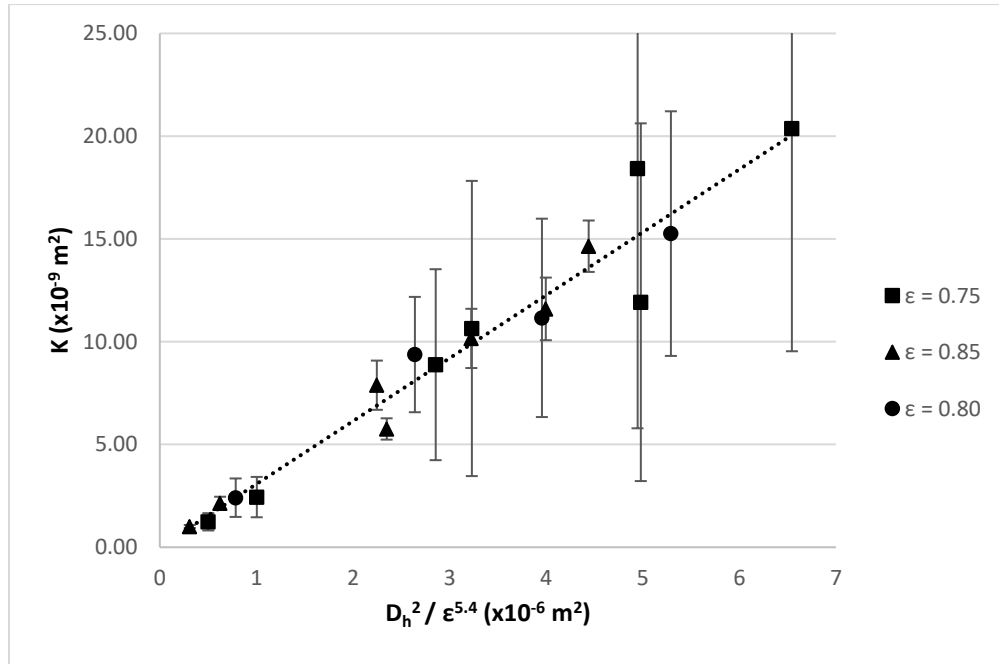


Figure 18. Plot of the permeability calculated using the numerical results as a function of the square of the hydraulic radius divided by porosity raised to the power of 5.4.

A least-squares regression analysis was performed on the data in Figure 18 to find an expression for permeability. The resulting P-value for the intercept of the least-squares line is 0.98, meaning that the intercept is likely zero and must be thrown out of the curve fit. When the intercept is set to zero, the regression analysis with a 95% confidence interval results in a slope of 3.07 ± 0.19 and a $0.985 R^2$ correlation coefficient value. The residuals for the curve fit in Figure 19 are random and have a mean close to zero, indicating the model is appropriate and there are no additional effects that need to be accounted for.

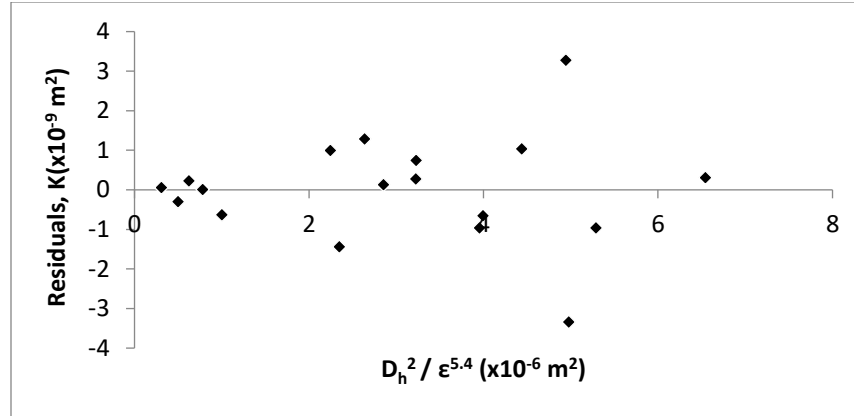


Figure 19. Residuals for the least-squares linear curve fit for the permeability model in equation (6.23).

Using the results from the regression analysis, the following expression for the permeability of graphite foam is proposed:

$$K = \frac{D_h^2}{326\epsilon^{5.4}} \quad (6.23)$$

where K is in units of m^2 and D_h in units of meters. Using the 95% confidence interval reported for the slope, the 95% confidence interval for the coefficient in equation (6.24) is 326 ± 19 . Using the definition for hydraulic radius in equation (2.15), the expression can be written in the following form:

$$K = \frac{1}{20.4\beta^2\epsilon^{3.4}} \quad (6.24)$$

The permeability expression in equation (6.24) depends only on the geometry of the graphite foam. When the pore diameter, inter-pore window diameter, and porosity of the foam are known the idealized geometry expression for β in Table 5 can be used in combination with equation (6.24) to estimate the permeability.

The proposed expression for permeability is comparable to expressions for the permeability packed beds. As mentioned in section 2.6.1, the Hagen-Poiseuille equation is a commonly used

expression for the permeability of packed beds. If the Kozeny constant of 5 is used for packed beds, the dimensionless permeability is

$$K_{DE} = \frac{K}{d^2} = \frac{\varepsilon^3}{180(1 - \varepsilon)^2} \quad (6.25)$$

To compare the permeability expression in the current study to the one for packed beds, the equivalent diameter introduced in section 2.6.1 will be used. The dimensionless form of the proposed expression for graphite foam is found by using the equivalent diameter expression in equation (2.4) and substituting for β in equation (6.24).

$$K_{DE} = \frac{K}{D_E^2} = \frac{1}{734.4(1 - \varepsilon)^2 \varepsilon^{3.4}} \quad (6.26)$$

Figure 20 shows a comparison between the dimensionless permeability using the equivalent particle diameter of the proposed expression for graphite foam and that of a packed bed of spherical particles for the porosity range included in this study. The dimensionless permeability of the graphite foam and packed beds are equal at $\varepsilon = 0.80$, but the value for graphite foam is greater at lower porosities and less at higher porosities. The porosity has a stronger effect on the permeability of packed beds than on that of graphite foam. A possible explanation for this is the range of opening sizes fluid must travel through in packed beds compared to graphite foam. In graphite foam the fluid passages will generally range in size from the window diameter to the pore diameter. In packed beds, however the flow passages are relatively wide between spheres, but shrink down to zero if the spheres are touching. The rapid variation in flow area is more profound at lower porosities and could explain the difference from graphite foam. The differences in dependence on porosity are not surprising, since the microstructure of graphite foam creates a drastically different flow pattern than packed beds. However, the differences are not severe (about 50% in K_{DE} at $\varepsilon = 0.75$ and 0.85) and show that the behavior predicted by the present model for permeability is

consistent with models in literature for other porous media. Further, Figure 20 shows that the extension of the Carman-Kozeny theory to flow through graphite foam is not effective since the internal structure is drastically different than packed beds and the effect of porosity on permeability is not correctly captured.

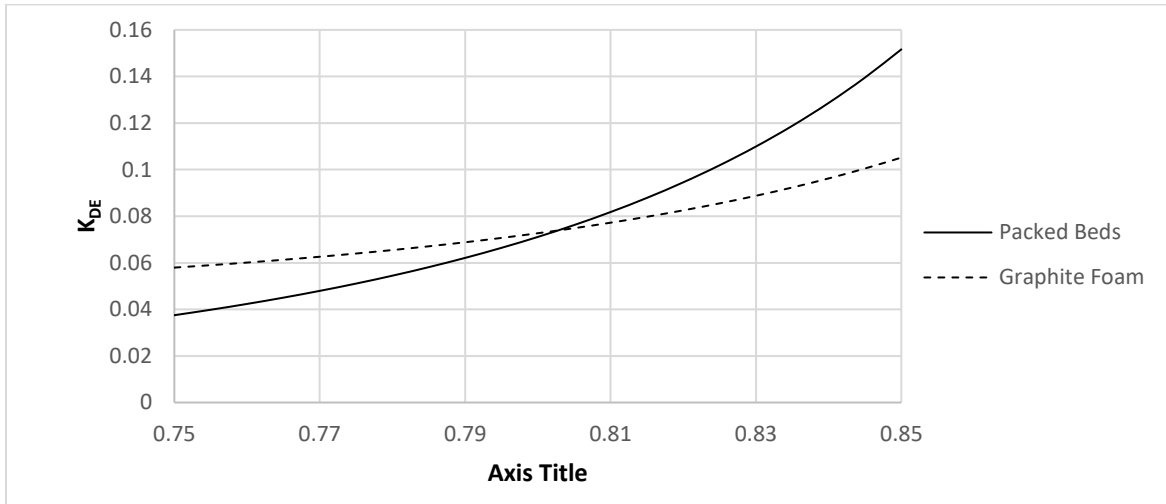


Figure 20. Comparison of the dimensionless permeability of the proposed expression for graphite foam using an equivalent particle diameter with that of a packed bed of spherical particles.

6.2.2 Form Coefficient Model

As discussed earlier, it is believed that the inertial effects on pressure drop in graphite foam are dominated by the sudden contraction and expansion the fluid experiences as it travels through the inter-pore windows. This is analogous to flow through an orifice or a sudden contraction and expansion in a pipe. Pressure drop correlations for flows through orifices as well as sudden contraction and expansion are well documented. The pressure loss coefficient across both is strongly dependent on the value of the ratio of the large diameter to small diameter [56]. Extending this behavior to flow through graphite foam, the value of the inertia coefficient is expected to be a function of the ratio of pore to window diameter, D_p/D_w . Figure 21 shows the results for the inertia coefficient as a function of D_p/D_w for various porosities.

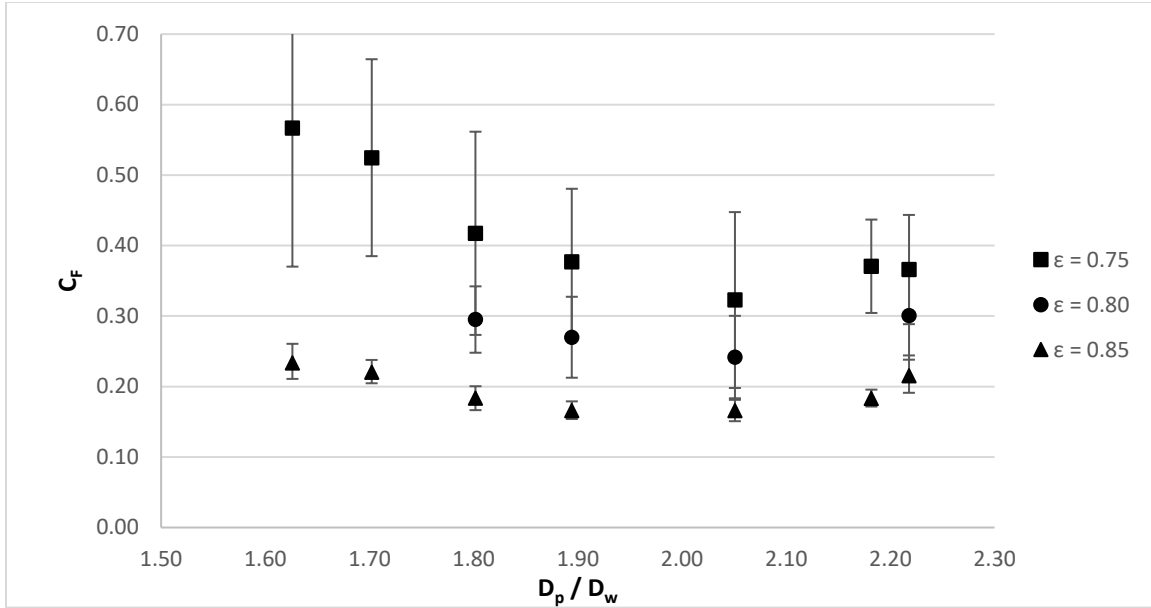


Figure 21. Plot of inertial coefficient from numerical results as a function of the ratio of pore to window diameter, D_p/D_w .

As expected, Figure 21 shows a strong dependence of the form coefficient on the value of D_p/D_w .

The porosity also has an effect on the form coefficient. Multiple regression analysis was performed to obtain an expression for the form coefficient as a function of the porosity and D_p/D_w ratio. As

a first guess, the following terms were used in the regression analysis: ϵ , $\frac{D_p}{D_w}$, $\epsilon \frac{D_p}{D_w}$, ϵ^2 , and $\left(\frac{D_p}{D_w}\right)^2$.

When all five terms are included, as well as an intercept, the resulting P-values for the ϵ and ϵ^2 terms are 0.20 and 0.86, respectively. This means that these terms could be zero. The P-values for the remaining terms were all well below 0.05, meaning they are significant and should be kept.

For the next trial, the ϵ^2 term was thrown out, but the ϵ term was kept, since the $\epsilon \frac{D_p}{D_w}$ term is significant and it is good practice to include single terms if they are included in an interaction term [54]. The results of this analysis, performed using Microsoft Excel, are shown in Table 13.

Table 13. Results of multiple regression analysis using Microsoft Excel used to model the form coefficient as a function of porosity and pore diameter to window diameter ratio.

<i>Regression Statistics</i>						
Multiple R	0.9927					
R Square	0.9854					
Adjusted R Square	0.9809					
Standard Error	0.0163					
Observations	18.0000					
<i>ANOVA</i>						
	<i>df</i>	<i>SS</i>	<i>MS</i>	<i>F</i>	<i>Significance F</i>	
Regression	4.0000	0.2332	0.0583	219.1345	8.7214E-12	
Residual	13.0000	0.0035	0.0003			
Total	17.0000	0.2366				
<i>Terms</i>	<i>Coefficients</i>	<i>Standard Error</i>	<i>t Stat</i>	<i>P-value</i>	<i>Lower 95%</i>	<i>Upper 95%</i>
Intercept	10.6069	0.7609	13.9398	3.3983E-09	8.9631	12.2508
D_p/D_w	-6.4145	0.5517	-11.6263	3.0513E-08	-7.6064	-5.2226
ε	-7.6965	0.7856	-9.7967	2.2821E-07	-9.3938	-5.9993
$D_p/D_w * \varepsilon$	2.8276	0.4053	6.9762	9.6796E-06	1.9519	3.7032
$(D_p/D_w)^2$	1.0267	0.1151	8.9216	6.6476E-07	0.7781	1.2753

By removing the ε^2 term from the model, the significance of the ε term, as indicated by its P-value, was greatly increased. Constant porosity curves from the resulting model using the coefficient in Table 13 are shown in Figure 22. These curves fall within the range of uncertainty of the numerical results, indicating that the model is a good fit. In addition, the correlation coefficients and the P-values for each term in Table 13 indicate that the proposed model is a good fit for the data. The residuals of the model must also be checked. As seen in Figure 23, the residuals for each term in the model have a mean of zero, show no trends, and are homoscedastic, meaning the vertical spread does not vary too much along the horizontal length of the plot. This means that it is very likely that the assumptions of the linear model are valid [54].

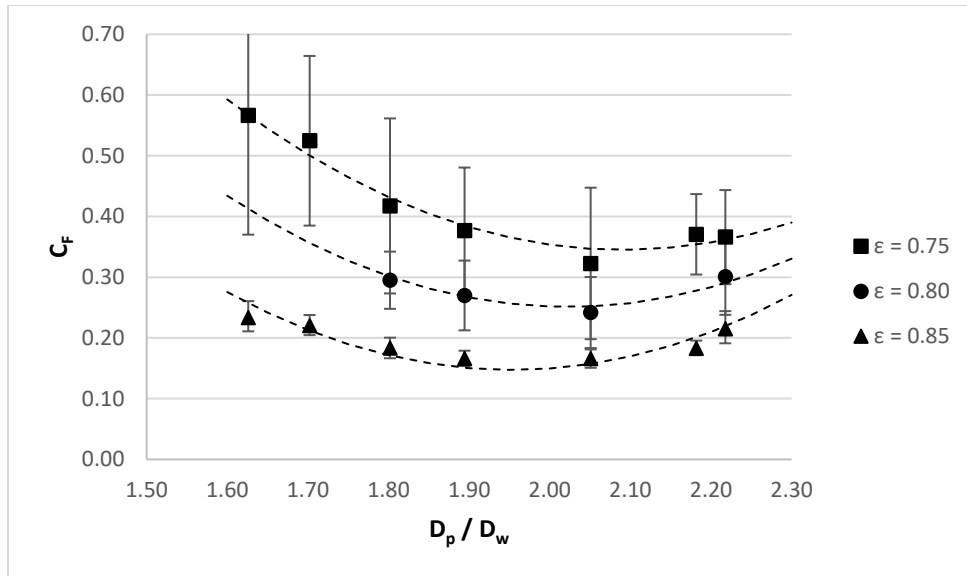


Figure 22. Constant porosity curves for the proposed model as a function of pore to window diameter ratio overlaid with results from the numerical simulations.

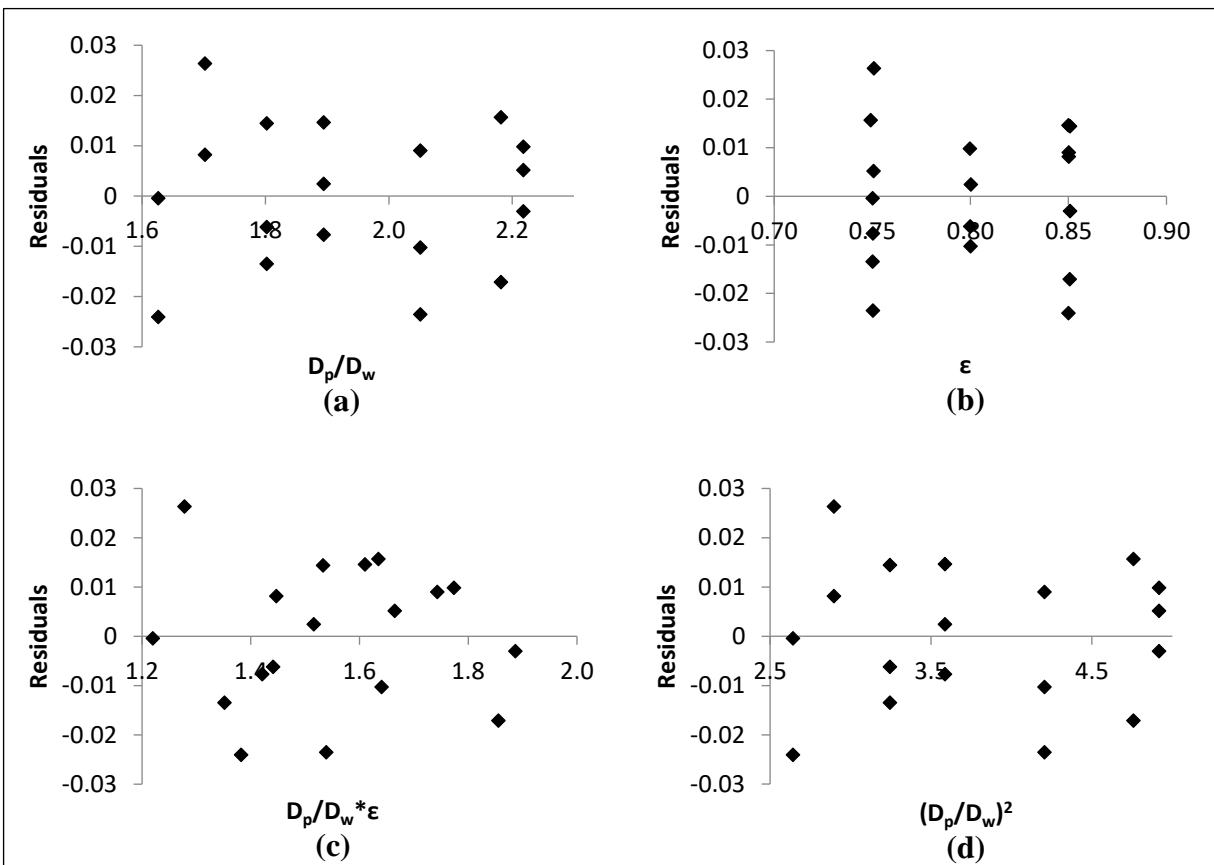


Figure 23. Residual plots for each term in the multiple regression model for the form coefficient: (a) D_p/D_w , (b) ϵ , (c) $D_p/D_w * \epsilon$, and (d) $(D_p/D_w)^2$

Now that the linear model was proven to be valid, the following expression for the form coefficient is proposed:

$$c_F = 10.61 - 6.41 \frac{D_p}{D_w} - 7.70\varepsilon + 2.83 \frac{D_p}{D_w} \varepsilon + 1.03 \left(\frac{D_p}{D_w} \right)^2 \quad (6.27)$$

Several interesting observations can be made by looking at the model curves in Figure 22. The form coefficient is minimized at a D_p/D_w value between 1.9 and 2.1, depending on the porosity. At high flow rates, the form coefficient dominates the total pressure drop. If this term can be minimized for a given porosity by adjusting the value of D_p/D_w , pressure drop due to inertial effects could be reduced. The model curves in Figure 22 also show a diminishing effect of porosity on the form coefficient as D_p/D_w increases. As the ratio D_p/D_w increases, the inertial losses associated with the contraction and expansion through the windows have an increasing effect on the total inertial losses. If the model is extended to higher D_p/D_w values, a point would be reached where the porosity curves converge and the form coefficient is independent of the porosity.

6.2.3 Summary

Expression for the permeability and form coefficient of graphite foam as functions of pore geometry were developed using linear regression analysis with the results of the numerical simulations. Both the permeability and form coefficient can be calculated using these expressions if the pore diameter, inter-pore window diameter, and porosity of the graphite foam is known. The value of the surface area density, β can be calculated using equation (3.29). A summary of these expressions along with their limitations are shown in Table 14.

Table 14. Summary of expressions for permeability and form coefficient of graphite foam as a function of foam geometry along with the limitations of these expressions.

Limitations	$1.63 < \frac{D_p}{D_w} < 2.22$ $15 < Re_h < 300$ $0.75 < \varepsilon < 0.85$
Permeability Model	$K = \frac{1}{20.4\beta^2\varepsilon^{3.4}} \quad (6.24)$
Form/Inertia Coefficient Model	$c_F = 10.61 - 6.41 \frac{D_p}{D_w} - 7.70\varepsilon + 2.83 \frac{D_p}{D_w} \varepsilon + 1.03 \left(\frac{D_p}{D_w} \right)^2 \quad (6.27)$

CHAPTER 7

CONCLUSION

High porosity graphite foam is an attractive option for various convective heat transfer applications because of its high thermal conductivity, high surface area per unit volume, low density, low coefficient of thermal expansion, and resistance to corrosion. One of the obstacles to the widespread application of graphite foam in heating and cooling applications is the relatively high pressure drop associated with flow through the foam. The goal of the current study was to provide insight into the effect of the foam microstructure on pressure drop by developing correlations for pressure drop coefficients as functions of pore microstructure parameters.

Specifically, a study was performed to develop correlations for the permeability and form coefficient of graphite foam as functions of internal pore geometry using the results from computational fluid dynamics simulations for air flow through idealized geometry models. The idealized geometry model used is similar to one used in previous studies with certain improvements. The numerical simulations were validated using experimental results in literature. The validity of the correlations are limited to the ranges of values for Reynolds number, porosity, and pore diameter to window diameter ratio that were included in the study.

An expression was presented for the permeability of graphite foam as a function of porosity and the surface area per unit volume. The permeability expression has a similar form as previous models developed for flow through packed beds of spheres. However, the permeability expression for graphite foam shows a weaker dependence upon porosity than expressions for packed beds of spheres. This difference is likely due to the sharp contrasts in microstructure and fluid flow path between packed beds and graphite foam.

The proposed expression for the form coefficient is unlike any other expression proposed in literature. The model expresses the form coefficient as a function of pore diameter to window diameter ratio, D_p/D_w , and the porosity, ε . The coefficient varies with the square of the pore diameter to window diameter ratio and is minimized at a D_p/D_w ratio between 1.9 and 2.1, depending on the value of porosity. In addition, at high D_p/D_w the form coefficient is less dependent upon porosity and the inertial losses associated with the contraction and expansion of the fluid through the inter-pore windows dominates the total inertial losses.

CHAPTER 8

FUTURE WORK

High porosity graphite foams demonstrate promising properties for convective heat transfer applications where weight and space constraints are important design factors. The current study aims to provide insight into the effect of graphite foam microstructure on hydraulic losses, which are an important factor in most convective heat transfer problems. The pressure drop correlations presented in the present study can be used in future studies that model graphite foam using the volume averaged method for computational fluid dynamics simulations. Further, these simulations can be used to optimize the values of pore diameter, inter-pore window diameter, and porosity for a specific application.

The numerical simulations used in the current study were validated using a small sample of experimental measurements for pressure drop in graphite foam. The data used was the only set available where all three of the necessary microstructure parameters (pore diameter, inter-pore window diameter, and porosity) were measured and reported. More experimental data for pressure drop is needed that measures all three of these values for the samples tested. Additional measurements can be used to modify, refine and validate the expressions proposed in the current study, and even extend the limitations of these expressions to wider ranges for porosity and pore diameter to window diameter ratio.

A better understanding of the effect of microstructure on pressure drop in graphite foam can lead to more wide spread applications for graphite foam in industry. However, the current process used to manufacture these foams is not precise enough to control the microstructure dimensions to a level that would ensure optimal performance. Further studies are required from the manufacturing perspective on how the microstructure can be controlled by adjusting the

processing parameters. In addition, progress must be made to reduce the cost associated with making these foams. The combination of reducing production costs and the ability to tailor foams to specific applications could lead to the widespread application of graphite foams in a variety of heating and cooling applications.

REFERENCES

REFERENCES

- [1] Klett, J.W., et. al., 2004, *The role of structure on the thermal properties of graphitic foams*, Journal of Material Science, Vol. 39, pp. 3659-3676.
- [2] Gallego, C.N., and Klett, W.J., 2003, *Carbon Foams for Thermal Management*, Carbon, Vol. 41, pp. 1461-1466.
- [3] Chen, C., Kennel, E., Stiller, A., Stansberry, P., & Zondlo, J., 2006, *Carbon foam derived from various precursors*. Carbon, 44(8), 1535-1543.
- [4] Klett, J.W. et al., 2000, *High-thermal-conductivity, mesophase-pitch-derived carbon foams: effect of precursor on structure and properties*, Carbon, Volume 38, Issue 7, Pages 953–973.
- [5] Klett, J.W., 2000, *Process for making carbon foams*, U.S. patent 6033506
- [6] Lin, Y.R, Du, J.H., Wu, W., Chow, L.C. 2010. *Experimental Study on Heat Transfer and Pressure Drop of Recuperative Heat Exchangers Using Carbon Foam*. ASME Journal of Heat Transfer. Vol. 132.
- [7] Aboelsoud, W., Wu, W. Chow, L.C., Saarloos, B.A., Rini, D.P., 2014, *Experimental Investigation of Thermal and Hydraulic Performance of V-Shape Corrugated Carbon Foam*, ASME Journal of Heat Transfer, Vol. 136.
- [8] Wu, W., Du, J.H., Lin, Y.R., and Chow, L.C., 2011, *Evaluation of Compact and Effective Air-Cooled Carbon Foam Heat Sink*, ASME Journal of Heat Transfer, Vol. 133
- [9] Wu, W., Du, J.H., Lin, Y.R., and Chow, L.C., 2009, *Design and Experiment of Compact and Effective Carbon Foam Recuperative Heat Exchangers*, Journal of Thermophysics and Heat Transfer, Vol. 23, No. 2, pp. 339-345.
- [10] Klett, J.W., Tee, C.C., Stinton, D.P., and Yu, N.A., 2000, *Heat Exchangers Based on High Thermal Conductivity Graphite Foam*, Proceedings of the 1st World Conference on Carbon: Eurocarbon 2000, 9-13 July, Berlin, Germany, pp. 449-450.
- [11] Garrity, Patrick T., Klausner, James F., and Mei, Renwei, 2010, *Performance of Aluminum and Carbon Foams for Air Side Heat Transfer Augmentation*, ASME Journal of Heat Transfer, Vol. 132.
- [12] Leong, K.C., Li, H.Y., Jin, L.W, Chai, J.C., 2009, *Numerical and experimental study of forced convection in graphite foams of different configurations*, Applied Thermal Management, Vol. 30, pp. 520-532.

REFERENCES (continued)

- [13] Straatman, A.G., Gallego, N.C., Yu, Q., Betchen, L., and Thompson, B.E., 2007, *Forced Convection Heat Transfer and Hydraulic Losses in Graphitic Foam*, ASME Journal of Heat Transfer, Vol. 129, pp. 1237-1245.
- [14] Wu, W., Du, J., Lin, Y.R., Kapat, J., and Chow, L.C., 2009, *Heat Transfer Enhancement of Gas-Cooled Condenser Using Carbon Foam*, Journal of Thermophysics and Heat Transfer, Vol. 23, No. 1, pp. 157-161.
- [15] Thompson, Brian E. 2014. *Heat Transfer in Porous Graphite Foams*. ASME Journal of Heat Transfer. Vol. 136.
- [16] Solmus, Ismail. 2014. *Numerical investigation of heat transfer and fluid flow behaviors of a block type graphite foam heat sink inserted in a rectangular channel*. Applied Thermal Engineering. Vol. 78, p 605-615.
- [17] Betchen, L.J. and Straatman, A.G., 2010, *An investigation of the effects of a linear porosity distribution on on-equilibrium heat transfer in high-conductivity graphite foam*, Numerical Heat Transfer, Part A, 58: 605-624.
- [18] Karimian, S.A. and Straatman, A.G., 2008, *CFD study of the hydraulic and thermal behavior of spherical-void-phase porous materials*, International Journal of Heat and Fluid Flow, Vol. 29, Issue 1, pp. 292-305
- [19] Yu, Q., Thompson, B.E., and Straatman, A.G., 2006, *A Unit Cube-Based Model for Heat Transfer and Fluid Flow in Porous Carbon Foam*, ASME Journal of Heat Transfer, Vol. 128, pp 352-360.
- [20] Karimian, S.A. and Straatman, A.G., 2009, *Numerical Modeling of Multidirectional Flow and Heat Transfer in Graphitic Foams*, ASME Journal of Heat Transfer, Vol. 131, 052602.
- [21] Degroot, C.T., and Straatman, A.G., 2012, *Numerical Results for the Effective Flow and Thermal Properties of Idealized Graphite Foam*, ASME Journal of Heat Transfer, Vol. 134, 042603.
- [22] Druma, A.M., Alam, M.K., 2006, *Surface Area and Conductivity of Open-Cell Carbon Foams*, Journal of Minerals and Materials Characterizations and Engineering, Vol. 5, No. 1, pp 73-86.
- [23] Druhma, C., et al., 2004, *Finite element model of thermal transport in carbon foams*, Journal of Sandwich Structures and Materials, Vol. 6, pp. 527-540.

REFERENCES (continued)

- [24] Tee, C.C., Yu, N., and Li, H., 2008, *Modeling the overall heat conductive and convective properties of open-cell graphite foam*, Modelling and Simulation in Material Science and Engineering, Vol. 16.
- [25] Sihn, S. and Roy, A.K., 2004, *Modelling and prediction of bulk properties of open-cell carbon foam*, Journal of Mechanics and Physics of Solids, Vol. 52, pp. 167-191.
- [26] Chai, Y. et al., 2016, *Study of Micro-Structure Based Effective Thermal Conductivity of Graphite Foam*, Proceedings of the ASME 2016 5th International Conference on Micro/Nanoscale Heat and Mass Transfer, January 4-6, 2016, Biopolis, Singapore.
- [27] Li, K., et al., 2005, *Micromechanical modeling of three-dimensional open-cell foams using the matrix method for spatial frames*, Composites, Vol. 36, Issue 3, pp. 249-262.
- [28] Kaviany, M., *Principles of Heat Transfer in Porous Media*, New York, Springer-Verlag New York Inc., 1991.
- [29] Civan, Faruk, *Porous Media Transport Phenomena*, Hoboken, New Jersey, John Wiley and Sons Inc., 2011.
- [30] Lage, J. L., 1998, *The Fundamental Theory of Flow Through Permeable Media From Darcy to Turbulence*, Transport Phenomena in Porous Media (eds. D. B. Ingham and I. Pop), pp.1-30, Pergamon, Oxford.
- [31] Nield, D. A., 2002, *Modelling Fluid Flow in Saturated Porous Media and at Interfaces*, Transport Phenomena in Porous Media (eds. D. B. Ingham and I. Pop), pp.1-19, Pergamon, Oxford.
- [32] Nield, D. A. and Bejan A., 2013, *Convection in Porous Media*, Fourth Ed., Springer, New York.
- [33] Norton, T.H., 2003, *Modeling of Corrugated Graphite Foam Heat Exchangers*, Thesis, University of Tennessee Knoxville.
- [34] Osgood, S. J., 2001, *Heat Transfer in Carbon Foam*, Thesis, Rensselaer Polytechnic Institute.
- [35] Dupuit, J., 1863, *Etudes Theoriques et Pratiques sur le Mouvement des Eaux*, Dunod, Paris.
- [36] Forchheimer, P., 1901, *Wasserbewegung durch Boden*, VDI Z., 45, 1782-1788.
- [37] Ergun, S., 1952, *Fluid Flow through Packed Columns*, Chemical Engineering Progress, Vol. 48, No. 2, pp. 89-94.

REFERENCES (continued)

- [38] Ward, J. C., 1964, *Turbulent Flow in Porous Media*, Journal of the Hydraulics Division (ASCE), Vol. 90, pp. 1-12.
- [39] Beavers, G. S. and Sparrow, E.M., 1969, *Non-Darcy Flow Through Fibrous Porous Media*, ASME Journal of Applied Mechanics, Vol. 36, pp. 711-714.
- [40] Hunt, M.L. and Tien, C.L., 1988, *Effects of thermal dispersion on forced convection in fibrous media*, Int. Journal of Heat and Mass Transfer, Vol. 31, No. 2, pp. 301-309.
- [41] Brinkman, H.C., 1947, *A calculation of the viscous force exerted by a flowing fluid on a dense swarm of particles*, Applied Scientific Research, Vol. A1, pp. 27-34.
- [42] Joseph, D.D., Nield, D.A., and Papanicolaou, G., 1982, *Nonlinear Equation Governing Flow in Saturated Porous Medium*, Water Resources Research, Vol. 18, No. 4, pp. 1049-1052.
- [43] Vafai, K. and Tien, C. L., 1981, *Boundary and Inertia Effects on Flow and Heat Transfer in Porous Media*, International Journal of Heat and Mass Transfer, Vol. 24, pp. 195-203.
- [44] Muskat, M., 1937, *Flow of Homogeneous Fluids through Porous Media*, McGraw-Hill, New York.
- [45] Vafai, K. and Kim, S. J., 1989, *Forced Convection in a Channel Filled With a Porous Medium: An Exact Solution*, Journal of Heat Transfer, Vol. 111, pp.1103-1106.
- [46] Philipse, A. P. and Schram, H. L., 1991, *Non-Darcian Airflow through Ceramic Foams*, Journal of American Ceramic Society, Vol. 74, No. 4, pp. 728-732.
- [47] Lage, J. L., 1998, *The Fundamental Theory of Flow Through Permeable Media From Darcy to Turbulence*, Transport Phenomena in Porous Media (eds. D. B. Ingham and I. Pop), pp.1-30, Pergamon, Oxford.
- [48] Carman, P.C., 1937, *The determination of the specific surface area of powder I*, J. Soc. Chem. Ind., 57, pp. 225-234.
- [49] Dybbs, A. and Edwards, R. V., 1984, *A new look at porous media fluid mechanics – Darcy to turbulent*, in *Fundamental of Transport Phenomena in Porous Media*, Bear and Corapcioglu, edg., Martinus Nijhoff Publishers, 199-254.
- [50] Beer, F.P. et al, 2010, *Vector Mechanics for Engineers Statics*, 9th ed., McGraw Hill, New York, New York.

REFERENCES (continued)

- [51] Hoffmann, K.A. and Chaing, S.T., 2000, *Computational Fluid Dynamics*, 4th ed., Engineering Education System, Wichita, Kansas.
- [52] Ansys Fluent User's Guide
- [53] Incropera, F.P. et al., 2007, *Fundamental of Heat and Mass Transfer*, 6th ed., John Wiley and Sons, Hoboken, NJ.
- [54] Navidi, W., 2011, *Statistics for Scientists and Engineers*, 3rd ed., McGraw Hill, New York, New York.
- [55] Mei, C., Auriault, J.L., 1991, *The effect of weak inertia on flow through a porous medium*, Journal of Fluid Mechanics, 222, pp. 647-663.
- [56] Cengel, Y.A. and Cimbala, J.M., 2010, *Fluid Mechanics Fundamental and Applications*, McGraw Hill, New York, New York.
- [57] Taylor, J.R., 1997, *An introduction to error analysis*, University Science Books, Sausalito, CA.
- [58] Anghelescu, M.S., 2009, *Thermal and Mechanical Analysis of Carbon Foam*, Dissertation, Ohio University.
- [59] Leong, K.C., and Li, H.Y., 2011, *Theoretical study of the effective thermal conductivity of graphite foam based on a unit cell model*, International Journal of Heat and Mass Transfer, Vol. 54, pp. 5491-5496.
- [60] Straatman, A.G., Gallego, N.C., Yu, Q., and Thompson, B.E., 2007, *Characterization of Porous Carbon Foam as a Material for Compact Recuperators*, ASME Journal of Heat Transfer, Vol. 129, pp. 326-330.
- [61] Taylor, G.I., 1971, *A Model for the Boundary Condition of a Porous Material: Part 1*, Journal of Fluid Mechanics, Vol. 49, Issue 2, pp. 319-326.
- [62] Lin, W., Yuan, J., and Sunden, B., *Review on graphite foam as a thermal material for heat exchangers*, World Renewable Energy Congress 2011, 8-11 May, 2011, Linkoping, Sweden
- [63] Druma, C., Alam, M.K. and Druma, A.M., 2004, *Finite Element Model of Thermal Transport in Carbon Foams*, Journal of Sandwich Structures and Materials, Vol. 6, pp. 527-540.

APPENDICES

APPENDIX A

NUMERICAL RESULTS

Table 15. Pressure loss per unit length as a function of fluid velocity for the numerical results from the present study.

Sample	$\epsilon = 0.75$		$\epsilon = 0.80$		$\epsilon = 0.85$	
	U (m/s)	$\Delta P/L$ (kPa/m)	U (m/s)	$\Delta P/L$ (kPa/m)	U (m/s)	$\Delta P/L$ (kPa/m)
2A	0.011	0.32	n/a		0.013	0.27
	0.022	0.64			0.025	0.54
	0.109	3.22			0.128	2.71
	0.326	10.09			0.383	8.61
	0.542	17.96			0.573	13.69
	0.870	32.36			0.955	25.94
	1.195	49.75			1.138	33.05
	1.521	70.11			1.526	49.01
	2.064	110.34			1.907	67.06
	2.390	138.35			2.288	87.02
	2.715	169.64			2.668	108.91
	3.040	204.71			3.049	132.87
	3.413	250.00			3.442	160.00
	3.842	310.00			3.964	200.00
	4.281	380.00			4.540	250.00
	4.724	460.00			5.152	310.00
	5.168	550.00			5.787	380.00
	5.613	650.00			6.436	460.00
	6.095	770.00			7.094	550.00
	6.569	900.00			7.754	650.00
7.247	1105.50	8.406	759.13			
7.966	1348.30	9.071	881.80			
8.706	1624.00	9.710	1011.60			

APPENDIX A (continued)

Table 15 (continued). Pressure loss per unit length as a function of fluid velocity for the numerical results from the present study.

Sample	$\epsilon = 0.75$		$\epsilon = 0.80$		$\epsilon = 0.85$	
	U (m/s)	$\Delta P/L$ (kPa/m)	U (m/s)	$\Delta P/L$ (kPa/m)	U (m/s)	$\Delta P/L$ (kPa/m)
3A	0.006	0.09	0.008	0.10	0.007	0.08
	0.013	0.19	0.057	0.72	0.018	0.20
	0.107	1.57	0.172	2.23	0.123	1.35
	0.322	5.09	0.344	4.79	0.368	4.47
	0.566	10.11	0.804	13.99	0.556	7.40
	0.942	20.21	1.378	30.13	0.926	14.58
	1.318	33.01	1.953	50.91	1.296	23.41
	1.694	48.41	2.528	77.33	1.666	33.65
	2.069	66.86	3.103	110.79	2.036	45.31
	2.445	89.07	3.678	152.05	2.406	58.60
	2.821	115.62	4.253	201.75	2.775	73.72
	3.177	145.00	4.828	260.73	3.228	95.00
	3.595	185.00	5.404	329.66	3.776	125.00
	4.046	235.00	5.980	408.80	4.399	165.00
	4.589	305.00	6.556	497.73	5.061	215.00
	5.128	385.00			5.734	275.00
	5.678	476.63			6.271	330.88
6.214	575.59			6.825	396.92	
3B	0.004	0.02			0.005	0.02
	0.022	0.12			0.027	0.11
	0.111	0.63			0.135	0.57
	0.276	1.80			0.336	1.68
	0.446	3.40			0.541	3.17
	0.555	4.66			0.744	5.00
	0.755	7.50			0.928	6.93
	0.943	10.81			1.317	11.93
	1.332	20.02			1.514	15.00
	1.527	26.00			1.705	18.35
	1.719	32.76			2.095	26.39
	2.108	49.34			2.288	31.00
	2.496	69.72			2.482	36.05
	2.714	83.00			2.676	41.50
	2.884	94.14			2.871	47.41
	3.166	114.54			3.062	53.63
	3.432	135.68			3.257	60.43

APPENDIX A (continued)

Table 15 (continued). Pressure loss per unit length as a function of fluid velocity for the numerical results from the present study.

Sample	$\epsilon = 0.75$		$\epsilon = 0.80$		$\epsilon = 0.85$	
	U (m/s)	$\Delta P/L$ (kPa/m)	U (m/s)	$\Delta P/L$ (kPa/m)	U (m/s)	$\Delta P/L$ (kPa/m)
4B	0.003	0.01	n/a		0.004	0.01
	0.012	0.03			0.014	0.03
	0.058	0.17			0.071	0.15
	0.116	0.35			0.143	0.33
	0.333	1.36			0.285	0.77
	0.550	2.95			0.410	1.28
	0.767	5.21			0.551	1.96
	0.984	8.26			0.793	3.40
	1.194	12.00			0.987	4.83
	1.419	16.97			1.229	7.00
	1.649	23.00			1.424	9.10
	1.853	29.20			1.654	12.00
	2.080	37.00			1.861	15.01
	2.287	45.07			2.074	18.50
	2.504	54.40			2.299	22.63
	2.608	59.08			2.514	27.00
4C	0.004	0.01	0.005	0.01	0.004	0.01
	0.018	0.03	0.039	0.07	0.021	0.03
	0.081	0.16	0.128	0.25	0.096	0.15
	0.172	0.39	0.523	1.63	0.203	0.35
	0.308	0.83	0.907	3.89	0.385	0.82
	0.452	1.44	1.292	7.29	0.578	1.45
	0.579	2.10	1.676	11.93	0.817	2.40
	0.857	4.00	2.071	18.11	1.028	3.42
	1.033	5.61	2.446	25.41	1.264	4.80
	1.283	8.50			1.477	6.27
	1.486	11.40			1.695	8.00
	1.698	15.00			1.926	10.10
	1.939	19.81			2.160	12.50
	2.163	25.00			2.374	14.96
	2.392	30.94			2.461	16.03

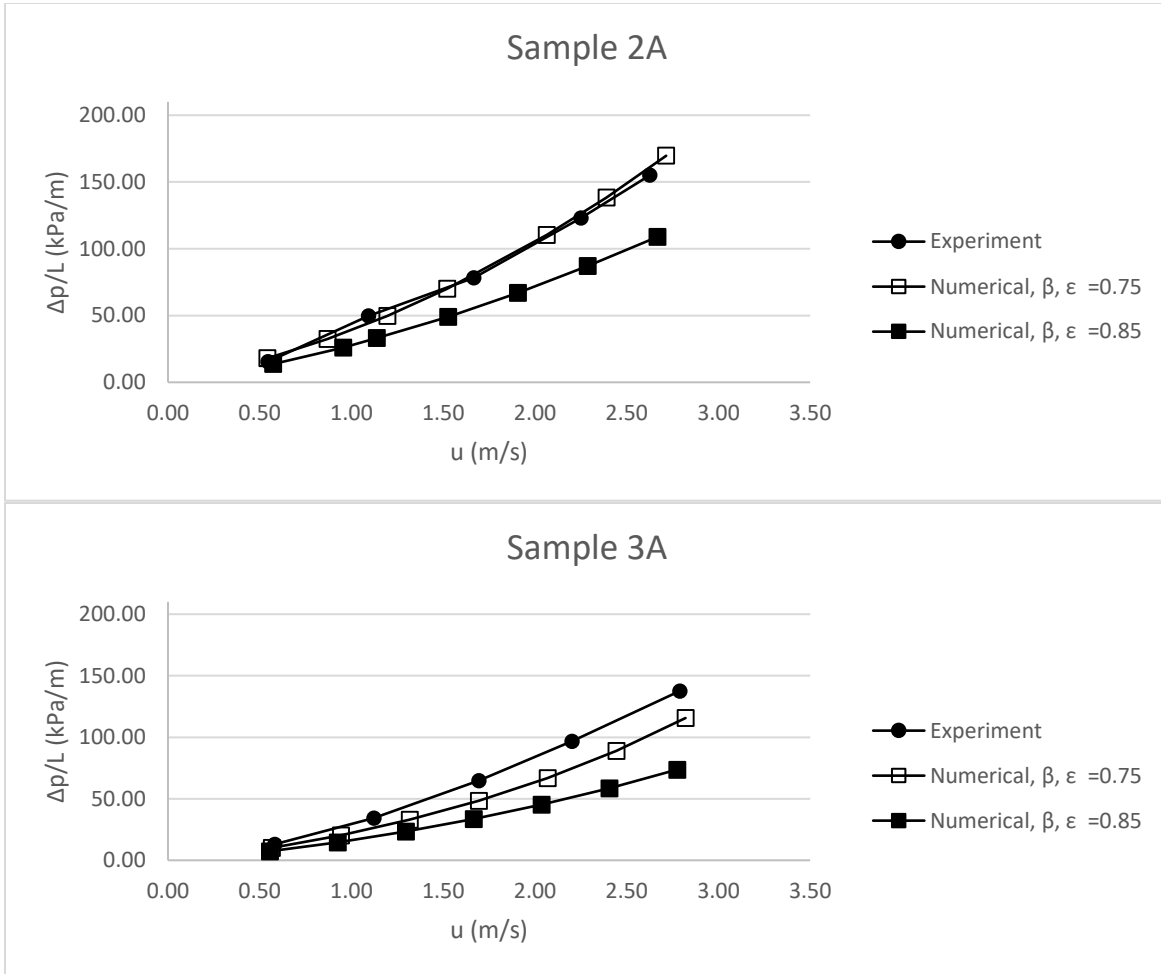
APPENDIX A (continued)

Table 15 (continued). Pressure loss per unit length as a function of fluid velocity for the numerical results from the present study.

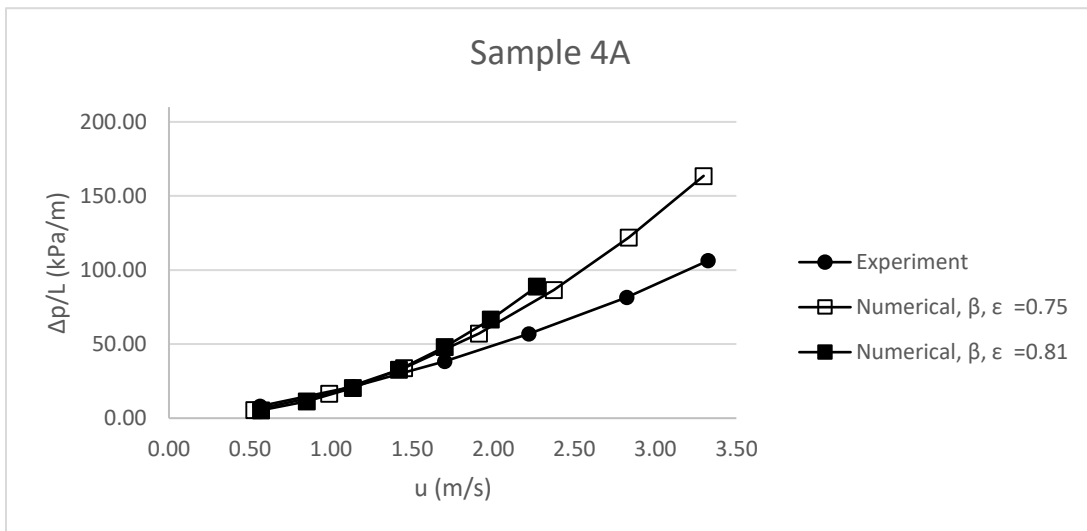
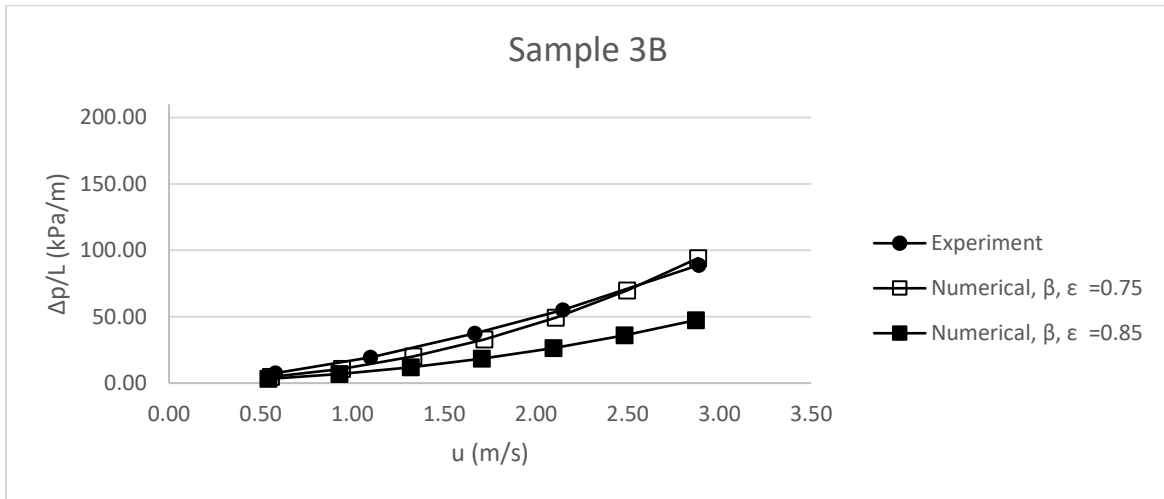
Sample	$\epsilon = 0.75$		$\epsilon = 0.80$		$\epsilon = 0.85$	
	U (m/s)	$\Delta P/L$ (kPa/m)	U (m/s)	$\Delta P/L$ (kPa/m)	U (m/s)	$\Delta P/L$ (kPa/m)
U1	0.007	0.03	0.008	0.03	0.009	0.02
	0.073	0.28	0.080	0.26	0.066	0.19
	0.183	0.76	0.201	0.73	0.185	0.57
	0.439	2.36	0.321	1.32	0.726	3.42
	0.696	4.69	0.602	3.15	1.258	7.81
	1.238	12.43	0.884	5.63	1.790	14.04
	1.762	24.55	1.165	8.81	2.322	22.33
	2.287	41.67	1.446	12.85	2.854	32.74
	2.812	64.09	1.727	17.82	3.387	45.40
	3.076	77.37	2.008	23.76		
	3.336	91.63	2.290	30.69		
			2.571	38.67		
			2.852	47.76		
			3.134	58.01		
		3.415	69.44			
U2	0.005	0.01	0.005	0.01	0.005	0.01
	0.046	0.13	0.050	0.12	0.053	0.11
	0.149	0.45	0.161	0.42	0.160	0.36
	0.459	1.90	0.570	2.21	0.533	1.71
	0.918	5.43	1.025	5.34	1.013	4.30
	1.377	11.16	1.481	10.02	1.493	7.97
	1.838	19.70	1.937	16.60	1.973	12.91
	2.298	31.38	2.393	25.32	2.453	19.25
	2.758	46.22	2.849	36.34	2.934	27.12

APPENDIX B

COMPARISON OF NUMERICAL AND EXPERIMENTAL RESULTS



APPENDIX B (continued)



APPENDIX B (continued)

